With the support of the Erasmus+ Programme of the European Union

# Erasmus Mundus Joint Master Degree "InterMaths" Interdisciplinary Mathematics

*Specialisation: Computational Fluid Dynamics in Industry (TUW, Vienna)*

| *Máster Universitario Erasmus Mundus en "Matemáticas Interdisciplinarias"* | *Laurea Magistrale nella classe LM-44 "Mathematical Modelling"* | *Master in "Interdisciplinary Mathematics"* |
|---|---|---|
| UNIVERSITAT AUTÒNOMA DE BARCELONA (UAB) | UNIVERSITÀ DEGLI STUDI DELL'AQUILA (UAQ) | TECHNISCHE UNIVERSITÄT WIEN (TUW) |

## Master's Thesis Title

*Investigating Snap-Through Dynamics in Bistable MEMS based on Buckled Elastic Structures*

**Supervisor**
Univ.Prof. Dipl.-Phys. Dr.rer.nat. Ulrich Schmid

**Candidate**
Orion Forowycz

**Co-advisor**
Univ.Ass. Daniel Platz

Student ID (UAQ): 280260

**Academic Year** 2022/2023

TECHNISCHE UNIVERSITÄT WIEN
Vienna University of Technology

# Investigating Snap-Through Dynamics in Bistable MEMS based on Buckled Elastic Structures

MASTERARBEIT

zur Erlangung des akademischen Grades

**Master of Science**

im Rahmen des Studiums

**Interdisciplinary Mathematics**

eingereicht von

**Orion Forowycz**
Matrikelnummer 12143744

an der Fakultät für Mathematik und Geoinformation

der Technischen Universität Wien

Betreuung: Univ.Prof. Dipl.-Phys. Dr.rer.nat. Ulrich Schmid
Mitwirkung: Univ.Ass. Daniel Platz, MSc PhD

Wien, 23. August 2023

Orion Forowycz

Ulrich Schmid

TECHNISCHE UNIVERSITÄT WIEN
Vienna University of Technology

# Investigating Snap-Through Dynamics in Bistable MEMS based on Buckled Elastic Structures

MASTER'S THESIS

submitted in partial fulfillment of the requirements for the degree of

**Master of Science**

in

**Interdisciplinary Mathematics**

by

**Orion Forowycz**
Registration Number 12143744

to the Faculty of Mathematics and Geoinformation

at the TU Wien

Advisor: Univ.Prof. Dipl.-Phys. Dr.rer.nat. Ulrich Schmid
Assistance: Univ.Ass. Daniel Platz, MSc PhD

Vienna, 23rd August, 2023

Orion Forowycz

Ulrich Schmid

# Declaration of Authorship

Orion Forowycz

I hereby declare that I have written this Master Thesis independently, that I have completely specified the utilized sources and resources and that I have definitely marked all parts of the work - including tables, maps and figures - which belong to other works or to the internet, literally or extracted, by referencing the source as borrowed.

Vienna, 23rd August, 2023

Orion Forowycz

# Abstract

We conducted an in-depth exploration of snap-through behavior in bistable Micro-Electro-Mechanical Systems (MEMS), using piezoelectric microplates as our representative system. Under several assumptions, including that the plate was thin and homogeneous, models for the plate deflections were derived from von Karman plate theory, coupled to a strain compatibility equation. The complexity of the partial differential equation (PDE) system was managed through the Galerkin method, transforming it into interconnected nonlinear ordinary differential equations (ODEs). Using a Python framework for numerical solutions, we investigated the effects of various piezoelectric tones on snap-through behaviors. The nuanced relationship between tone combinations and their impact on snap-through timing was highlighted. Certain dual tones could accelerate, delay, enable, or completely inhibit snap-through. These insights offer avenues for more controlled, efficient, and innovative applications in MEMS devices, particularly where rapid snap-through is essential.

# Contents

CHAPTER 1

# Introduction

In the expansive landscape of microtechnology, Micro-Electro-Mechanical Systems (MEMS) stand out as a landmark innovation. Over the past few decades, MEMS have seamlessly woven themselves into the fabric of numerous applications. As their name implies, MEMS devices are characterized by being on the scale of micrometers, but their applications are anything but small [1].

The electro-mechanical basis of MEMS helps differentiate between the two main categories of MEMS applications: sensors and actuators. Each rely on a different approach to harness the potential of MEMS. Sensors, as their name implies, are used to record mechanical and physical quantities such as acceleration, pressure, and temperature as electrical signals. Actuators, on the other hand, use electrical signals to induce mechanical motion [2] [3]. A great example of the applications of actuators are MEMS speakers, in which an AC voltage causes an actuator to vibrate an acoustic diaphragm that produces sound waves. MEMS speakers may be able to outperform conventional speakers by being smaller, more energy efficient, and having greater potential to be directly integrated with electronic circuits in batches [4].

MEMS actuators are characterized by their deflection behavior, which is how the shape of the actuator deforms with or without stimuli. These actuators can be classified into two categories based on their deflection behavior at rest: monostable and bistable [5]. Monostable actuators have a single stable deflection state. Due to

the elastic nature of the actuator, the deflection will eventually return to this state if there is ever a deviation from said state, barring any external stimuli. Bistable MEMS actuators, on the other hand, have two stable deflection states which can be on the scale of tens of micrometers as the result of a pre-stress of the actuator material. These bistable deflections can be much larger than the deflections of monostable actuators, which are typically on the scale of nanometers [6]. Given that the purpose of actuators is to move in order to perform a task, a greater deflection ability can be a significant advantage.

Since bistable MEMS devices have two stable states, these devices can switch between these states in a process known as snap-through [7]. One way to achieve these states is known as buckling. However, instead of harnessing the potential benefits of snap-through's change in deflection, much of the existing research has been focused on mitigating or avoiding it [8]. A primary concern is the nonlinear dynamics exhibited during the snap-through process, which makes this process harder to predict and control. Therefore, a better understanding of the snap-through process is needed to better utilize bistable MEMS devices.

To induce the snap-through, a transduction mechanism is needed to convert electrical input signals into excitations that can trigger the snap-through. Several options include electrostatic, magnetic, thermal, and piezoelectric methods. [9]. For this project, we focus on the piezoelectric method, whereby a layer of piezoelectric material is deposited onto the surface of the actuator. When a voltage signal is applied to the piezoelectric layer, it changes the stress within the piezoelectric material and thus the actuator as a whole, which then causes the deflection to change. If the change in deflection is large enough, snap-through occurs. Existing experimental research has demonstrated that the piezoelectric method has the potential to be effective at inducing snap-through with low energy consumption [9] [10] .

In this project, we aim to better understand the snap-through phenomenon in piezoelectrically-induced bistable MEMS devices using a mathematical model and numerical simulations. We consider the MEMS device to be a thin, square plate subject to a given piezoelectric excitation. We assume that the material of the plate is homogeneous, elastic, and isotropic. We set the pre-stress of the plate to be at a level that induces bistability.

To model the plate, we use von Karman plate theory to form a system of partial differential equations (PDEs) that accounts for the nonlinearity due to large deflections. We incorporate a piezoelectric layer by modeling the layer as a time-dependent stress resultant that is added to the pre-stress resultant of the plate. An analytic solution to this system is not feasible due to the nonlinearity, so we use the Galerkin method to transform the PDE system into a set of coupled nonlinear ordinary differential equations (ODEs). We then use a Python-based simulation framework to numerically solve these ODEs via an explicit Runge-Kutta method of order 5(4).

We model the piezoelectric stress resultant (piezo-stress) as either a single- or dual-frequency tone. For the single-frequency tone, the piezo-stress is a sinusoidal function of time with a given frequency and amplitude. For the dual-frequency tone, the piezo-stress is the sum of two single-frequency tones, each with their own frequency and amplitude. We then subject the system to a variety of these single- or dual-frequency tones in order to analyze the resulting snap-through behavior.

In particular, we are interested in determining which piezo-stress tones efficiently induce snap-through. Thus, we simulate the deflection of the plate over time for a variety of piezo-stress tones and record how long it takes for snap-through to occur. Faster snap-through is desirable for several reasons. One, by reducing the time it takes for snap-through to occur, the MEMS device would be more responsive to the input signal. Thus it becomes easier to trigger the snap-through at a desired time. Two, the snap-through process is nonlinear, so the faster it occurs, the less time there is for nonlinear effects to accumulate and the easier it is to predict the behavior of the system. And three, the faster the snap-through occurs, the shorter the piezo tone has to be active and thus less energy is needed to induce snap-through. Thus, we can use the time it takes for snap-through to occur as a metric for the efficiency of the piezo-stress tone. Furthermore, lower-amplitude tones require less energy to produce, so we also consider the amplitude of the piezo-stress tone as a metric for energy-efficiency. Thus, we aim to find low-amplitude piezo-stress tones that quickly induce snap-through. Energy-efficiency presents us an especially important motivation due to the push for devices such as MEMS to require less energy, to allow for real-world devices to run longer with limited energy sources [10].

Existing computational research has explored the snap-through time of piezoelectric

plates subject to a single-frequency piezo-stress tone [6]. However, the snap-through time of piezoelectric plates subject to a dual-frequency piezo-stress tone had not yet been explored. Thus, we address this opportunity by exploring the snap-through time of piezoelectric plates subject to a dual-frequency piezo-stress tone, to understand whether these more-complex tones can be more efficient at inducing snap-through than single-frequency tones. In addition to varying the frequencies and amplitudes of the tone, we also explore the effect of a phase difference between the two frequencies of the overall tone. Lastly, also explore the effect of different linear damping rates on the snap-through time to understand how the time is effected as well as whether each dual-frequency tone remains efficient at inducing snap-through.

# CHAPTER 2

# Mathematical Model

## 2.1 von Karman Plate Theory

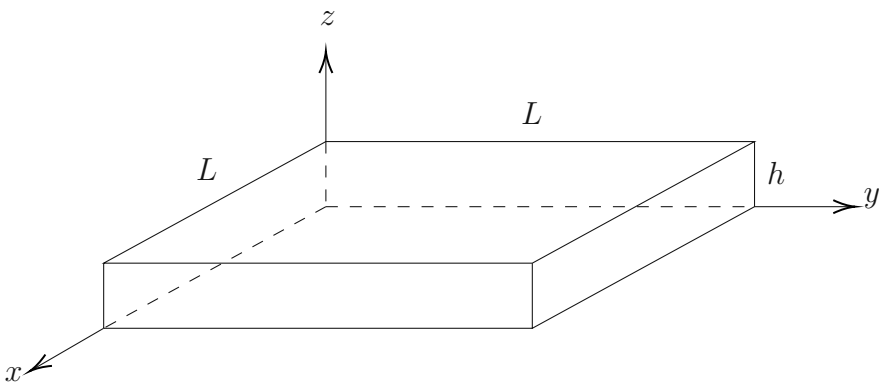


**Figure 2.1:** Schematic of the square plate.

We consider a square plate as depicted in Figure 2.1 with side length $L$ in the x,y-directions and thickness $h$ in the z-direction. We consider the plate to be relatively thin, i.e. $h \ll L$, and all the edges to be fixed in place. We allow the plate to have a deflection $w$ of such a plate in the z-direction, but we neglect any displacements in the x,y-directions due to the fixed boundary conditions. As for the material, we will assume that plate is entirely composed of silicon, and that the silicon is linearly elastic and isotropic.

By von Karman plate theory, the deflection $w$ of such a plate in the z-direction can be modeled with the following partial differential equation (PDE) [11] [6]

$$\mu\frac{\partial^2 w}{\partial t^2} + D\nabla^4 w - N_{xx}\frac{\partial^2 w}{\partial x^2} - N_{yy}\frac{\partial^2 w}{\partial y^2} - 2N_{xy}\frac{\partial^2 w}{\partial x \partial y} = 0 \tag{2.1}$$

where $\mu$ is the areal mass density $\mu = \rho h$ with density $\rho$ of the material. D is the flexural rigidity, given by

$$D = \frac{Eh^3}{12(1-\nu^2)} \tag{2.2}$$

where $E$ is Young's modulus and $\nu$ is Poisson's ratio. For a silicon plate that is isotropic and linearly thermoelastic, these properties have the values $E = 165 \times 10^9$ Pa and $\nu = 0.22$ [12]. $N_{xx}$, $N_{yy}$, and $N_{xy}$ are then the stress resultants which represent the in-plane stress of the system. Lastly, $\nabla^4$ is the two-dimensional biharmonic operator, defined as

$$\nabla^4 = \frac{\partial^4}{\partial x^4} + \frac{\partial^4}{\partial y^4} + 2\frac{\partial^4}{\partial^2 x \partial^2 y}. \tag{2.3}$$

Very importantly, Equation 2.1 highlights the direct relationship between the in-plane forces and the plate's deflection. By adjusting these stress resultants, which represent the in-plane forces, one modifies the plate's deflection behavior. However, these stress resultants are currently unknowns, resulting in a underdetermination of the system that needs to be addressed.

## 2.2 Airy Stress Function

To determine the stress resultants, we can model them using an Airy stress function $F = F(x, y)$ where [11]

$$\begin{aligned} N_{xx} &= \frac{\partial^2 F}{\partial y^2}, \\ N_{yy} &= \frac{\partial^2 F}{\partial x^2}, \\ N_{xy} &= -\frac{\partial^2 F}{\partial x \partial y}. \end{aligned} \tag{2.4}$$

Accordingly, we obtain the Airy von Karman nonlinear PDE

$$\mu\frac{\partial^2 w}{\partial t^2} + D\nabla^4 w - \frac{\partial^2 F}{\partial y^2}\frac{\partial^2 w}{\partial x^2} - \frac{\partial^2 F}{\partial x^2}\frac{\partial^2 w}{\partial y^2} + 2\frac{\partial^2 F}{\partial x \partial y}\frac{\partial^2 w}{\partial x \partial y} = 0 \tag{2.5}$$

This equation is coupled to a strain compatibility equation which imposes an additional condition to the Airy function such that [13]

$$\nabla^4 F = Eh\left(\left(\frac{\partial^2 w}{\partial x \partial y}\right)^2 - \frac{\partial^2 w}{\partial x^2}\frac{\partial^2 w}{\partial y^2}\right). \tag{2.6}$$

To model the energy dissipation as a result of a change in the deflection of the plate, we then add a linear damping term $\kappa\mu\frac{\partial w}{\partial t}$ to obtain

$$\mu\frac{\partial^2 w}{\partial t^2} + \kappa\mu\frac{\partial w}{\partial t} + D\nabla^4 w - \frac{\partial^2 F}{\partial y^2}\frac{\partial^2 w}{\partial x^2} - \frac{\partial^2 F}{\partial x^2}\frac{\partial^2 w}{\partial y^2} + 2\frac{\partial^2 F}{\partial x \partial y}\frac{\partial^2 w}{\partial x \partial y} = 0 \tag{2.7}$$

where $\kappa$ is the damping rate. With this damping term, we assume that the damping has a linear and homogeneous relation with the speed of deflection $\frac{\partial w}{\partial t}$.

## 2.3 Non-Dimensionalisation of PDE

To reduce the number of parameters and to make the system more generalizable, a non-dimensionalization of the PDE was then performed. Thus, characteristic quantities were needed for each of the parameters to serve as a suitable non-dimensionalization factor. For the x and y dimensions, the side length $L$ was the characteristic length used to form the non-dimensional coordinates

$$\bar{x} = \frac{x}{L} \qquad \bar{y} = \frac{y}{L} \tag{2.8}$$

For the deflection $w$ however, the side length is relatively large compared to the typically deflections, so the plate thickness $h$ was more suitable for forming the non-dimensional deflection

$$\bar{w} = \frac{w}{h} \tag{2.9}$$

The characteristic time $T$ can then provide a non-dimensional time

$$\bar{t} = \frac{t}{T}$$

To determine a expression for characteristic time $T$ suitable for non-dimensionalization, the first term of Equation 2.7 provided some insight. But first, we divided the whole equation by the flexural rigidity $D$ (units of $\mathrm{kg\,m^2\,s^{-2}}$) in order to have that become incorportated into the non-dimensionalization of time.

$$\frac{\mu}{D}\frac{\partial^2 w}{\partial t^2} + \frac{\kappa\mu}{D}\frac{\partial w}{\partial t} + \nabla^4 w - \frac{1}{D}\frac{\partial^2 F}{\partial y^2}\frac{\partial^2 w}{\partial x^2} - \frac{1}{D}\frac{\partial^2 F}{\partial x^2}\frac{\partial^2 w}{\partial y^2} + \frac{2}{D}\frac{\partial^2 F}{\partial x \partial y}\frac{\partial^2 w}{\partial x \partial y} = 0 \quad (2.10)$$

Now by substituting the non-dimensionalizations into the first term,

$$\frac{\mu}{D}\frac{\partial^2 w}{\partial t^2} = \frac{\mu}{D}\frac{\partial^2 (h\bar{w})}{\partial (T\bar{t})^2} = \frac{h\mu}{T^2 D}\frac{\partial^2 \bar{w}}{\partial \bar{t}^2} \quad (2.11)$$

and into the third term $\nabla^4 w$

$$\nabla^4 w = \frac{h}{L^4}\nabla^4 \bar{w}, \quad (2.12)$$

we then know the units of these terms must match, so

$$\frac{h\mu}{T^2 D} = \frac{h}{L^4} \quad (2.13)$$

$$\frac{\mu L^4}{D} = T^2 \quad (2.14)$$

$$T = \sqrt{\frac{\mu L^4}{D}} \quad (2.15)$$

As for the non-dimensionalization of the damping rate $\kappa$, this characteristic time $T$ can cancel out the unit of rate (per second) of the damping rate. By also incorporating $\mu$ into this non-dimensionalization, we can further simplify the PDE. Therefore, the non-dimensional damping rate is

$$\bar{\kappa} = \kappa\frac{T}{\mu} \quad (2.16)$$

For the terms with the Airy stress function, the $1/D$ coefficient can be cancelled out by setting the non-dimensional Airy function to be

$$\bar{F} = \frac{F}{D} \tag{2.17}$$

Using these non-dimensionalizations, we then can then form the non-dimensional PDE

$$\ddot{\bar{w}} + \bar{\kappa}\dot{\bar{w}} + \bar{\nabla}^4\bar{w} - \frac{\partial^2\bar{F}}{\partial\bar{y}^2}\frac{\partial^2\bar{w}}{\partial\bar{x}^2} - \frac{\partial^2\bar{F}}{\partial\bar{x}^2}\frac{\partial^2\bar{w}}{\partial\bar{y}^2} + 2\frac{\partial^2\bar{F}}{\partial\bar{x}\partial\bar{y}}\frac{\partial^2\bar{w}}{\partial\bar{x}\partial\bar{y}} = 0. \tag{2.18}$$

where $\ddot{w}$ and $\dot{w}$ are the non-dimensionalized second and first time derivatives of $w$, respectively. Furthermore, in cases where some stress resultant $N$ (such as $N_{xx}$, $N_{yy}$, etc) needs to be non-dimensionalized, the following equation can be used

$$\bar{N} = \frac{L^2}{D}N \tag{2.19}$$

since the square spatial units of $L^2$ cancels out the two spatial derivatives of $N$ as a function of $F$, as evidenced by Equation 2.4. To form a complete coupled system, we also need a non-dimensional version of the strain compatibility relation of Equation 2.6. Accordingly, using the definition $D = Eh^3/(12(1-\nu^2))$, the non dimensional strain compatibility equation becomes

$$\bar{\nabla}^4\bar{F} = 12(1-\nu^2)\left(\left(\frac{\partial^2\bar{w}}{\partial\bar{x}\partial\bar{y}}\right)^2 - \frac{\partial^2\bar{w}}{\partial\bar{x}^2}\frac{\partial^2\bar{w}}{\partial\bar{y}^2}\right) \tag{2.20}$$

## 2.4 Galerkin Method

Finding analytic solutions to the system of coupled nonlinear partial differential equations (PDEs) of Equations 2.18 and 2.20 is challenging; thus, we use a numerical approach to find the snap-through dynamics of the plate. We use a Galerkin method, whereby we assume the solution to be of the form

$$\bar{w}(\bar{t},\bar{x},\bar{y}) = q_i(\bar{t})\phi_i(\bar{x},\bar{y}) \tag{2.21}$$

where $q_i(t)$ are the generalized coordinates and $\phi_i$ are the Galerkin basis functions. This method allows us to transform the PDE system into a system of coupled

non-linear ordinary differential equations (ODEs). We chose to use 4 basis functions, in particular the modes $\phi_1, \phi_2, \phi_3, \phi_4$, which are shown in Figure 2.2. The decision to use 4 basis functions is derived from a earlier work that also used the Galerkin method to solve for the deflection of a plate based on von Karman theory [14]. This work indicated a significant difference in the results between using 1 versus 4 functions, but little difference between 4 and 9. Thus, under the assumption that the use of more basis functions can better encapsulate the variety of deflection behavior, but without having to make the simulation too complex by using too many basis functions without much change in the results, the number of basis functions was chosen to be 4. Similarly to that work [14], the basis functions were set to be of the form

$$\phi_i = (\cos((j-1)\pi x) - \cos((j+1)\pi x)(\cos((k-1)\pi y) - \cos((k+1)\pi y)$$

where the values of $j, k$ for each basis function are shown in Table 2.1

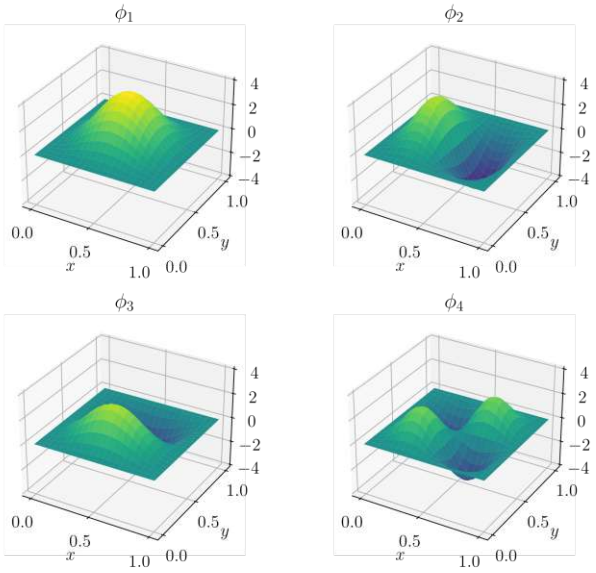


**Figure 2.2:** The basis functions $\phi_i$ corresponding to the 4 modes of the plate.

**Table 2.1:** Basis Function Indices

| Basis Function $\phi_i$ | j | k |
|---|---|---|
| 1 | 1 | 1 |
| 2 | 1 | 2 |
| 3 | 2 | 1 |
| 4 | 2 | 2 |

For each mode $i$, the maximum deflection $w_i$ over time is given by

$$w_i(t) = q_i \max_{\bar{x},\bar{y}\in[0,1]} \phi_i(\bar{x},\bar{y}) \tag{2.22}$$

This maximum deflection is useful for representing the deflection of the plate in a particular mode as one scalar value at a given time. The values of the maximums of the basis functions are detailed in Table 2.2.

**Table 2.2:** Maximum values of the basis functions $\phi_i$

| Mode $i$ | $\max_{\bar{x},\bar{y}\in[0,1]} \phi_i(\bar{x},\bar{y})$ |
|---|---|
| 1 | 4.00000 |
| 2 | 3.07919 |
| 3 | 3.07919 |
| 4 | 2.37036 |

We ascertain the Airy function $\bar{F}$ by dividing it into a homogeneous $\bar{F}_{\text{homog}}$ portion and inhomogeneous $\bar{F}_{\text{inhomog}}$ portion as follows

$$\bar{F} = \bar{F}_{\text{homog}} + \bar{F}_{\text{inhomog}} \tag{2.23}$$

For the homogeneous portion, we introduce a constant pre-stress resultant $N^{(0)}$ and a time-dependent piezo-stress resultant $N^{(p)}(\bar{t})$, where the second spatial derivatives of the stress resultant $N_{homog}$ corresponding to the homogeneous portion have the following form

$$N_{\bar{x}\bar{x}} = N_{\bar{y}\bar{y}} = N^{(0)} + N^{(p)}(t) \tag{2.24}$$

$$N_{\bar{x}\bar{y}} = 0 \tag{2.25}$$

By Equation 2.4, these derivatives imply that

$$\frac{\partial^2 \bar{F}_{\text{homog}}}{\partial \bar{x}^2} = \frac{\partial^2 \bar{F}_{\text{homog}}}{\partial y^2} = N^{(0)} + N^{(p)}(\bar{t}) \tag{2.26}$$

$$\frac{\partial^2 \bar{F}_{\text{homog}}}{\partial \bar{x} \partial \bar{y}} = 0 \tag{2.27}$$

And thus $\bar{F}_{\text{homog}}$ is of the form

$$\bar{F}_{\text{homog}} = \frac{\bar{x}^2 + \bar{y}^2}{2} \left( N^{(0)} + N^{(p)}(\bar{t}) \right)$$

As for the inhomogeneous portion $\bar{F}_{\text{inhomog}}$, we set this to be

$$\bar{F}_{\text{inhomog}} = f_{ijk} q_i(\bar{t}) q_j(\bar{t}) \phi_k(\bar{x}, \bar{y}) \tag{2.28}$$

where the coefficients $f_{ijk}$ are determined by inserting $\bar{F}_{\text{inhomog}}$ into the strain compatibility Equation 2.20. Therefore, the Airy function is then

$$\bar{F} = \frac{\bar{x}^2 + \bar{y}^2}{2} \left( N^{(0)} + N^{(p)}(\bar{t}) \right) + f_{ijk} q_i(\bar{t}) q_j(\bar{t}) \phi_k(\bar{x}, \bar{y}) \tag{2.29}$$

By inserting this Airy function (Equation 2.29) as well as the Galerkin representation of the deflection (Equation 2.21) into the non-dimensional PDE of Equation 2.18, we then obtain the following second-order system of ODEs

$$M_{ij} \ddot{q}_j + \bar{\kappa} M_{ij} \dot{q}_j + \left( K_{ij} + C_{ij} N^{(0)} + C_{ij} N^{(p)}(\bar{t}) \right) q_j + G_{ijkl} q_j q_k q_l = 0 \tag{2.30}$$

This system is contains four matrices/tensors. $M_{ij}$ is the mass matrix which encapsulates the areal mass density of the system, and this matrix has the coefficient values

$$M_{ij} = \int_\Omega \phi_i \phi_j \mathrm{d}\Omega \tag{2.31}$$

where the plate domain is $\Omega = [0, 1] \times [0, 1]$. $K_{ij}$ is the stiffness matrix which represents the resistance of the plate to deformation, and this matrix has the coefficient values

$$K_{ij} = \int_\Omega \phi_i \left( \frac{\partial^4}{\partial \bar{x}^4} \phi_j + \frac{\partial^4}{\partial \bar{y}^4} \phi_j + 2 \frac{\partial^4}{\partial^2 \bar{x} \partial^2 \bar{y}} \phi_j \right) \mathrm{d}\Omega. \tag{2.32}$$

$C_{ij}$ is the curvature matrix which shifts the stiffness of the modes due to the pre- and piezo-stress , and this matrix has the coefficient values

$$C_{ij} = -\int_{\Omega} \phi_i \left( \frac{\partial^2}{\partial \bar{x}^2} \phi_j + \frac{\partial^2}{\partial \bar{y}^2} \phi_j \right) \mathrm{d}\Omega. \tag{2.33}$$

$G_{ijkl}$ is the coupling tensor which describes the coupling between modes and themselves or other modes, and this tensor has the coefficient values

$$G_{ijkl} = -f_{jkm} \int_{\Omega} \phi_i \left( \frac{\partial^2 \phi_m}{\partial \bar{y}^2} \frac{\partial^2 \phi_l}{\partial \bar{x}^2} + \frac{\partial^2 \phi_m}{\partial \bar{x}^2} \frac{\partial^2 \phi_l}{\partial \bar{y}^2} - 2 \frac{\partial^2 \phi_m}{\partial \bar{x} \partial \bar{y}} \frac{\partial^2 \phi_l}{\partial \bar{x} \partial \bar{x}} \right) \mathrm{d}\Omega. \tag{2.34}$$

# CHAPTER 3

# Numerical Solution

## 3.1 Non-Dimensionalisation of Simulation Parameters

In order to be able to directly compare with the results of a previous work that dealt with a similar system, the values of the parameters used in the simulation were chosen in order to match those of the reference work [6]. The parameters used in that work for most of its simulations are given in Table 3.1 in dimensional form.

**Table 3.1:** Reference Dimensional Simulation Parameters from [6]

| Parameter | Value |
|---|---|
| Side Length $L$ | $700\,\mu m$ |
| Thickness $h$ | $3.5\,\mu m$ |
| Young's Modulus $E$ | $165\,GPa$ |
| Density $\rho$ | $2330.0\,kg\,m^{-3}$ |
| Damping Rate $\kappa$ | $700\,kg\,m^{-2}\,s^{-1}$ |
| Critical Stress $N_{cr}$ | $-66.55\,N\,m^{-1}$ |
| Simulation Time $\tau$ | $300\,\mu s$ |

For the Critical Stress $N_{cr}$ in particular, the value is determined from [6] to be

$$N_{cr} = -\frac{16\pi^2 D}{3L^2}. \tag{3.1}$$

The critical stress represents the value of the pre-stress at which the plate begins to buckle, that is, begin to deviate from zero deflection.

By using the non-dimensionalization equations from Section 2.3 on the values in Table 3.1, we then arrived at the non-dimensional simulation parameters listed in Table 3.2. From here on, consider all stated parameters and results to be in non-dimensional form unless otherwise specified.

**Table 3.2:** Non-Dimensional Simulation Parameters

| Parameter | Value |
|---|---|
| Damping Rate $\bar{\kappa}$ | 4.889 |
| Critical Stress $\bar{N}_{cr}$ | -52.64 |
| Simulation Time $\bar{\tau}$ | 5.3 |

## 3.2 Derivation of 1st Order ODE Systems

To reconstruct the system of equations of the system from the second-order ODE form of Equation 2.30 into a form that is solvable by methods, we represent the system as two sets of first-order ODEs. One set is based on the generalized coordinate (position) $q_j$ with time derivative $\dot{q}_j$, and the other based on the velocity $\dot{q}_j$ with time derivative $\ddot{q}_j$ (for modes $j \in \{1, 2, 3, 4\}$. Since the time derivative of position is simply velocity, the ODE for the position $q_j$ is

$$\frac{\partial}{\partial t} q_j = \dot{q}_j, \tag{3.2}$$

Next, we obtain the ODE for the velocity $\dot{q}_j$ by finding an expression for its time derivative $\ddot{q}_j$. To do this, we first multiply the left side of each term of Equation 2.30 by the inverse $(M^{-1})_{mi}$ of the mass matrix $M_{ij}$ as follows

$$\begin{aligned}
&(M^{-1})_{mi} M_{ij} \ddot{q}_j + \kappa (M^{-1})_{mi} M_{ij} \dot{q}_j \\
&+ \left( (M^{-1})_{mi} K_{ij} + (M^{-1})_{mi} C_{ij} N^{(0)} + (M^{-1})_{mi} C_{ij} N^{(p)}(t) \right) q_j \\
&+ (M^{-1})_{mi} G_{ijkl} q_j q_k q_l = 0
\end{aligned} \tag{3.3}$$

Rearranging the terms of the equation such that only the $\ddot{q}_m$ term is on the left

side, the equation becomes

$$(M^{-1})_{mi}M_{ij}\ddot{q}_m = -\left((M^{-1})_{mi}K_{ij} + (M^{-1})_{mi}C_{ij}N^{(0)} + (M^{-1})_{mi}C_{ij}N^{(p)}(t)\right)q_j - (M^{-1})_{mi}G_{ijkl}q_jq_kq_l - \kappa(M^{-1})_{mi}M_{ij}\dot{q}_j, \tag{3.4}$$

and with the mass matrix and its inverse then forming the Dirac delta function

$$(M^{-1})_{mi}M_{ij} = \delta^m_j \tag{3.5}$$

we obtain

$$\delta^m_j\ddot{q}_j = -\left((M^{-1})_{mi}K_{ij} + (M^{-1})_{mi}C_{ij}N^{(0)} + (M^{-1})_{mi}C_{ij}N^{(p)}(t)\right)q_m - (M^{-1})_{mi}G_{ijkl}q_jq_kq_l - \kappa\delta^m_j\dot{q}_j \tag{3.6}$$

Then by applying the delta functions, the system of ODEs for mode $m$ in a suitable form for numerical integration are then given by

$$\frac{\partial}{\partial t}q_m = \dot{q}_m \tag{3.7}$$

$$\frac{\partial}{\partial t}\dot{q}_m = -\left((M^{-1})_{mi}K_{ij} + (M^{-1})_{mi}C_{ij}N^{(0)} + (M^{-1})_{mi}C_{ij}N^{(p)}(t)\right)q_j - (M^{-1})_{mi}G_{ijkl}q_jq_kq_l - \kappa\dot{q}_m \tag{3.8}$$

where Equation 3.7 is an ODE of the position $q_m$ and Equation 3.8 is an ODE of the velocity $\dot{q}_m$. Since there are four modes, this results in a total of $4 \times 2 = 8$ equations. To record the state of this overall system, we arranged a state vector in the format of

$$\vec{s} = \begin{bmatrix} q_1 \\ \dot{q}_1 \\ q_2 \\ \dot{q}_2 \\ q_3 \\ \dot{q}_3 \\ q_4 \\ \dot{q}_4 \end{bmatrix} \tag{3.9}$$

with position elements $q_i$ for each node of the system in the even indices, and a velocity elements $\dot{q}_i$ for each node of the system in the odd indicies.

## 3.3 Python Framework

The function `integrate.solve_ivp` from the Python package `SciPy 1.8.0` was used to solve the system of ODEs. Upon providing a RHS (right hand side) function for the ODE system as well as a numerical method, tolerance values, a time range, and other parameters, the function returned a solution to the ODE system that we then processed to determine the deflection over time corresponding to each of the modes of the system. The numerical method used was the Runga-Kutta method of order (4)5, hereby referred to as RK45. The RHS function of the system returns the time derivative of the state vector (Equation 3.9) at a given time $t$.

The coefficient matrices $M_{ij}, C_{ij}, K_{ij}$ and tensor $G_{ijkl}$ were calculated using the Python package `SymPy 1.11.1`. The results were then saved for later use within the RHS function. To implement the RHS function, the derivatives of the position and velocity elements were needed, which were calculated using the Python package `NumPy 1.22.3` and the system as shown in Equations 3.7 and 3.8. To lower the execution time, some time-independent components of the system were pre-calculated outside of the RHS function and then referenced as needed. Algorithm 1 provides pseudocode for the pre-calculation when the system is initialized as a Python class. Then the Call function is the aforementioned RHS function.

**Algorithm 3.1:** von Karman Plate

**Data:** mass_matrix, damping_rate, stiffness_matrix, curvature_matrix, coupling_tensor, n0_vec, n_piezo

**Result:** Initialized vonKarmanAiry object

$n_{\text{modes}} \leftarrow$ shape of first dimension of *mass_matrix*

$n_{\text{dim}} \leftarrow 2 \times n_{\text{modes}}$

$n_{\text{order}} \leftarrow 2$

pos_indices $\leftarrow$ even indices in range $n_{\text{dim}}$

vel_indices $\leftarrow$ odd indices in range $n_{\text{dim}}$

Save matrices $mass\_matrix, stiffness\_matrix, curvature\_matrix, coupling\_tensor$

Save vector *n0_vec* as static_stress_vec

Save scalar *damping_rate*

static_stress_curvature_matrix $\leftarrow$ diagonal(*static_stress_vec*) $\times$ *curvature_matrix*

inverse_mass_matrix $\leftarrow$ inverse(*mass_matrix*)

Precompute terms

**Function** `Call(`*time, state_vector*`)`**:**

    Separate *state_vector* into *position_vector* and *velocity_vector*

    **if** *n_piezo_signal is None* **then**

        *n_piezo_signal_at_t* $\leftarrow 0$

    **else**

        *n_piezo_signal_at_t* $\leftarrow$ *n_piezo_signal*(*time*)

    **end**

    Update at_t_piezo_stress_matrix

    Update at_t_piezo_stress_term_inverse_mass

    Compute velocity_derivative

    Update state_derivative

    **return** state_derivative

## 3.4 Convergence Analysis

To use the RK45 solver, we needed to specify the relative tolerance (rtol) and absolute tolerance (atol) values. Furthermore, we needed to ensure that the solver was converging to a solution. Thus, we performed a convergence analysis of the solver by fixing the value of the atol to be $10^{-8}$ and varying the rtol from $10^{-4}$ to $10^{-10}$ while running reference simulations in non-dimensional form. These reference simulations modeled the piezo stress resultant to be a sinusoidal tone with amplitude $N_0^{(p)} = 10$ and frequency $f_p = 0.1$, and the rest of the parameters were set to their non-dimensionalized values as listed in Table 3.2.

The results of the convergence analysis are shown in Figure 3.1. For each value of rtol, a reference simulation was run, and the following $L_2$-norm was taken between the entire series of mode 1 deflections of the simulation with that rtol and the previous simulation (with the previous, higher rtol value). This $L_2$-norm was then plotted against the rtol value on a log-log scale in Figure 3.1. As the rtol decreases, the $L_2$-norm decreases, indicating that the solution is converging to a solution. Based on this analysis, we chose to use a rtol value of $10^{-8}$ for the rest of the simulations.

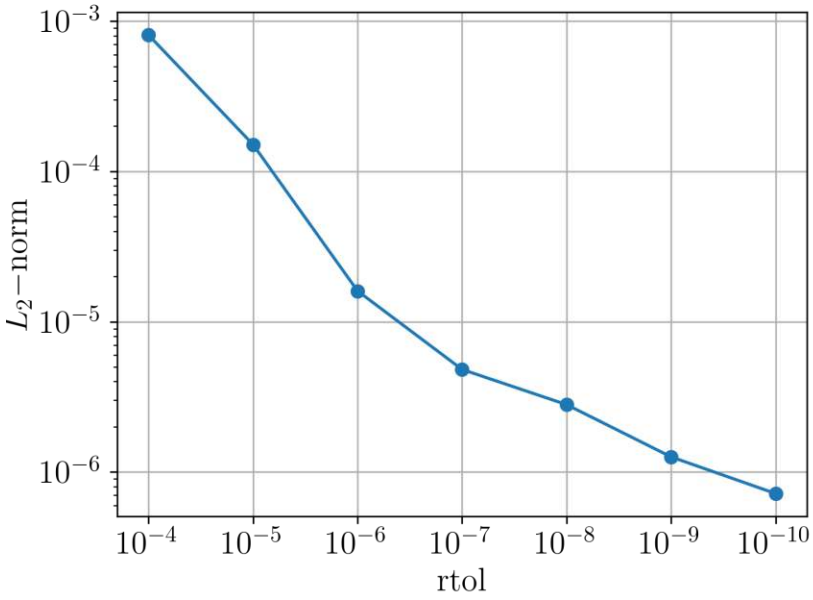


**Figure 3.1:** Convergence of RK45 as rtol decreases

Next, we performed the same process, but with the rtol fixed at $10^{-8}$ and varying the atol from $10^{-4}$ to $10^{-10}$. The results of this analysis are shown in Figure 3.2. As the atol decreases, the $L_2$-norm decreases, indicating that the solution is converging to a solution. Based on this analysis, we chose to use an atol value of $10^{-8}$ for the rest of the simulations.

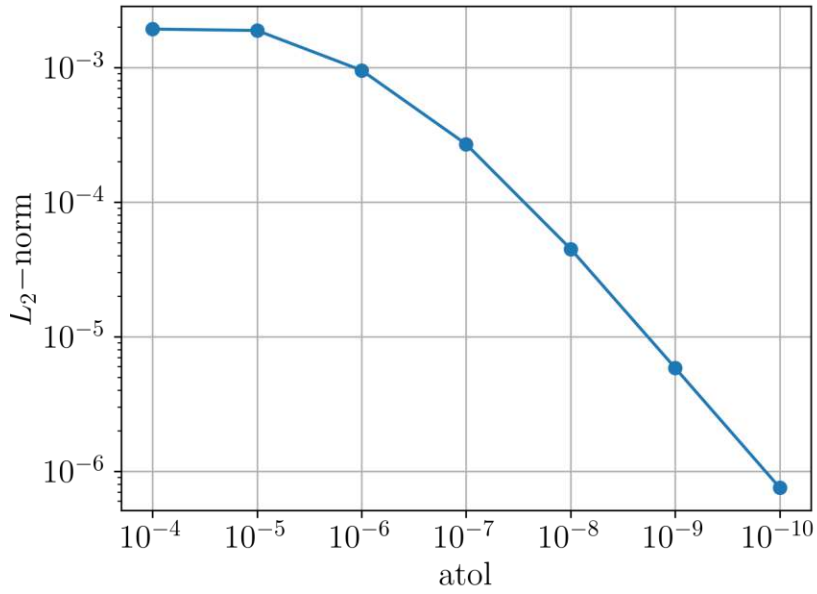


**Figure 3.2:** Convergence of RK45 as atol decreases

## 3.5 Event Detection

In our study, a significant emphasis was placed on understanding the precursor behaviors leading to the initial snap-through event during each simulation. Recognizing the value of optimizing computational resources and time, we incorporated an event detection algorithm specifically tailored for the `scipy.integrate.solve_ivp` function. This algorithm was designed to detect and halt the simulation once the mode 1 maximum deflection $w_1$ reached zero, signaling the occurrence of the first snap-through event.

Upon testing, it was observed that the event detection mechanism readily identified the initial snap-through event in each simulation. Moreover, the implementation

of the event detection algorithm led to a reduction in the time needed to run the simulation, roughly proportional to the time of the first snap-through event divided by the total simulation time without this event detection. For example, in a simulation lasting 4 time units, the event detection algorithm reduced the simulation time by approximately 50% when the first snap-through event occurred at 2 time units.

Owing to its efficiency and accuracy, the event detection algorithm became our tool of choice for simulations where the primary focus was the behavior leading up to the first snap-through event. However, in scenarios demanding insights into behaviors post the initial snap-through, we refrained from deploying the event detection algorithm, permitting the simulation to run for its complete duration.

CHAPTER 4

# System Analysis

## 4.1 Bifurcation of Static Deflections

In the broader context of our dynamic ODE system analysis, it is essential to first address the static behaviors inherent to the system. By analyzing the static aspects, we can establish the bistability of the system and identify the stable static deflections of the system. These static deflections serve as the starting point for the dynamic simulations, which can then perturbed to initiate the snap-through events.

To derive the equation representing the static portion of the system of Equations 3.7 and 3.8, we eliminated the time-dependent terms, which included the piezo-stress term and the terms with time derivatives. This exclusion leads to a simplified equation that encapsulates the position of the static system

$$0 = -\left((M^{-1})_{mi}K_{ij} + (M^{-1})_{mi}C_{ij}N^{(0)}\right)q_j - (M^{-1})_{mi}G_{ijkl}q_jq_kq_l. \qquad (4.1)$$

Within the purview of this equation, the only variables that are not predetermined are the generalized deflections, denoted by $q_i$, and the pre-stress resultant, symbolized by $N^{(0)}$. Thus, a significant implication is that by identifying the roots of this equation, one can ascertain the stable static deflections of the system, contingent on a specified pre-stress resultant.

To pinpoint these roots with precision, we utilized the `scipy.optimize.root` function. Due to the need for providing the function with an starting point, initial approximations of $q_i = 4$ and $q_i = -4$ were selected (non-dimensional). These served to determine positive and negative static deflections, respectively. With these initial values guiding the computational process, the function adeptly identified the roots, which were the system's stable static deflections.

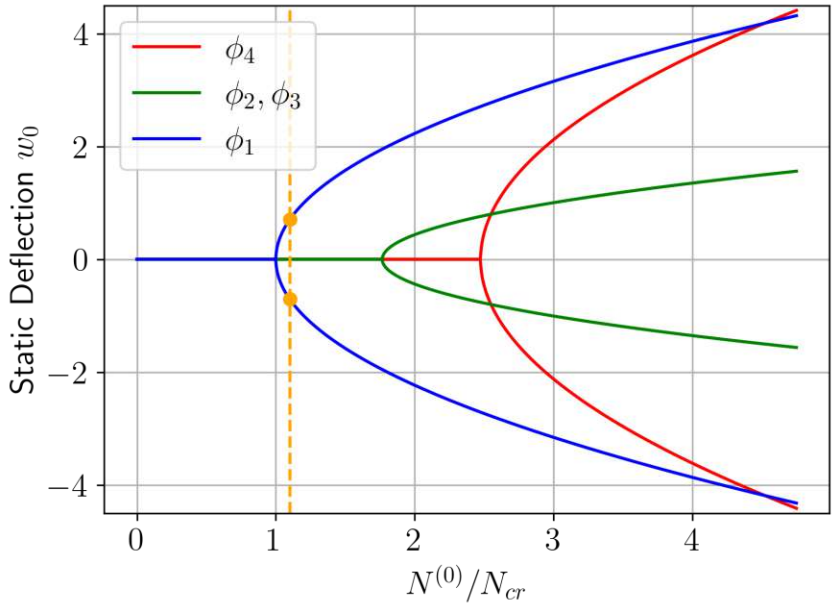


**Figure 4.1:** Bifurcation diagram of the static system.

In Figure 4.1, we present the bifurcation diagram of the static system. The x-axis illustrates the pre-stress resultant $N^{(0)}$ as a ratio of the critical stress $N_{cr}$, while the y-axis marks the static maximum deflection $w_i$ of mode $i$ for a given pre-stress condition (all non-dimensional). This static deflection is given by finding the roots of Equation 4.1 in generalized coordinates $q_i$, then multiplying them by the maximum of the basis function of the corresponding mode, as detailed by Equation 2.22. Each distinct mode of the system is depicted through a separate curve for clarity, labeled by the corresponding mode $\phi$. The blue curve represents the first mode, the green curve represents and second and third modes, and the red curve represents the fourth mode.

For scenarios where $N^{(0)}$ is less than $N_{cr}$, the static deflection of the first mode is at the origin, a fact evident from the blue curve. Upon reaching $N^{(0)} = N_{cr}$, a bifurcation in the deflection of the first mode emerges, signifying buckling. This observation further substantiates that our chosen non-dimensional value of $N_{cr}$ has been computed accurately. Following this threshold, i.e., for $N^{(0)} > N_{cr}$, the primary mode of the system deflects statically in one of two states, distinctly represented by the upper and lower blue trajectories.

An intriguing point of note is at $N^{(0)} = 1.1N_{cr}$, delineated by the intermittent orange line. Here, the system adopts a bistable stance, evidenced by the static deflection possibilities demarcated by the orange markers at $w = \pm 0.7059787$ (non-dimensional). We will use this value of the pre-stress, $N^{(0)} = 1.1N_{cr}$ for our dynamic simulations, since it exhibits the bistable behavior in the first mode that is necessary for snap-through, while the static deflection of the rest of the modes remains at zero. This is desirable in order to simplify the snap-through behavior of the system by primarily focusing on the first mode.

## 4.2 Static Deflection Verification

Transitioning from our analysis of the static system, we simulate the dynamic system. Leveraging the full dynamic system provides an avenue to verify the stable behavior at the observed static deflections. especially when the system begins its journey from the aforementioned static deflection points without any piezo-stress interference. For mode 1, its initial position was set to match the generalized coordinate equivalent of the static deflections, specifically at $w = \pm 0.7059787$. To add a realistic adjustment, we introduced a very small perturbation to every mode's position, equivalent to the non-dimensional representation of 1 nm.

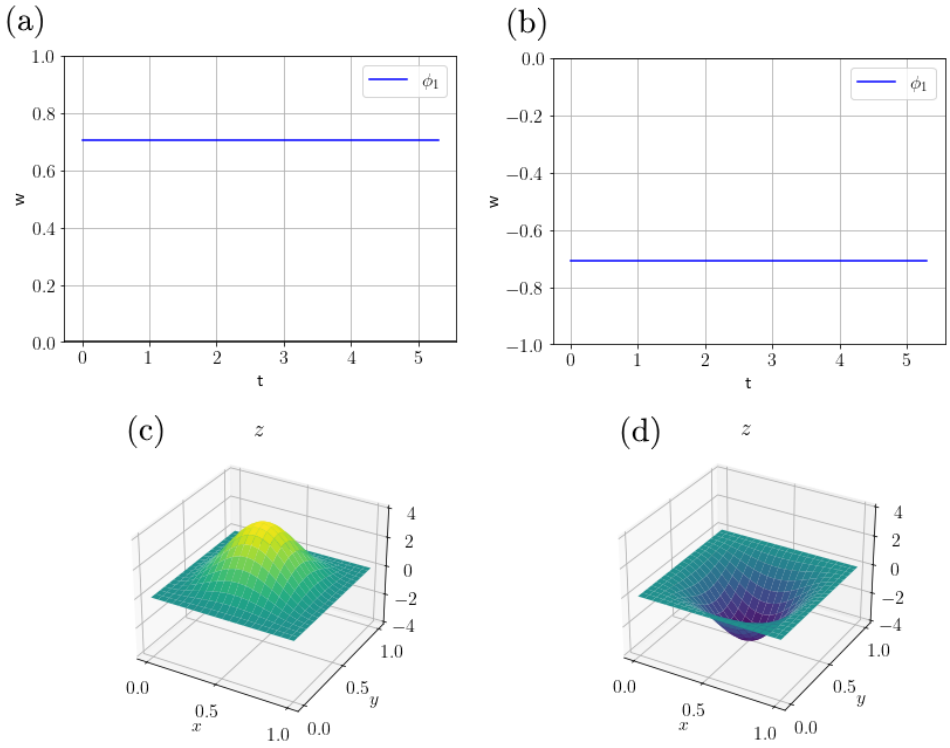


**Figure 4.2:** Bistable states of the system for $N^{(0)} = 1.1N_{cr}$

The ensuing system behavior is captured in Figure 4.2. Plots (a) and (b) show the maximum mode 1 deflection of the plate over time in non-dimensional units for the positive and negatively states respectively, whereas plots (c) and (d) illustrate how the plate is shaped in these states. Commencing from either the positive or negative static deflection points with the additional small perturbation, the deflection remained stable at that deflection, with only minor oscillations observed due to the perturbation. This behavior fortifies the assertion that the identified static deflection points are indeed resilient and stable points within the dynamic framework. Thus, the positive static deflection of mode 1 ($w_1 = 0.7059787$) will be used as the starting point for the snap-through simulations, with the addition of the small perturbation in the deflection of all modes to represent a more realistic scenario due to external disturbances.

# CHAPTER 5

# Results

## 5.1 Piezoelectric Excitation

To model the application of a single continuous piezoelectric excitation to the system (for instance as the result of a voltage signal), the piezo stress resultant was defined to be a single-frequency tone (single tone) of the form

$$N^{(p)}_{\text{single}}(t) = N^{(p)}_0 \sin(2\pi f_p t), \quad t \geq 0 \tag{5.1}$$

where the amplitude $N^{(p)}_0$ and frequency $f_p$ were constant over time, but their values were altered in different simulations to test to the system's response to a variety of possible tones. By using a sine-based tone, we can maintain that the tone is zero at $t = 0$ and avoid discontinuity.

In the dual-frequency tone case (dual tone), the piezo stress was redefined as the sum of two single tones as follows

$$N^{(p)}_{\text{dual}}(t) = N^{(p)}_1(t) + N^{(p)}_2(t), \quad t \geq 0 \tag{5.2}$$

where tone 1 was defined to be a single tone of the form

$$N^{(p)}_1(t) = N^{(p)}_{0,1} \sin(2\pi f_{p,1} t), \quad t \geq 0 \tag{5.3}$$

and tone 2 was defined to be a single tone of the form

$$N_2^{(p)}(t) = N_{0,2}^{(p)} \sin(2\pi f_{p,2} t + \varphi_p), \quad t \geq 0 \tag{5.4}$$

where $\varphi_p$ is a phase shift between the two tones. However, unless stated otherwise, $\varphi_p$ was set to be zero. In each batch of simulations, tone 1 was typically set to a specific frequency and amplitude. Tone 2 was then varied in frequency and amplitude to test the system's response to a variety of possible tones. This variation is done between one simulation and another. The frequency and amplitude of tone 2 however remain constant over time within each individual simulation.

## 5.2 Single Tone

Once a piezo tone is applied to the system, the maximum mode 1 deflection $w_1$ of the plate can deviate significantly from its static state over time. One such example is illustrated in Figure 5.1

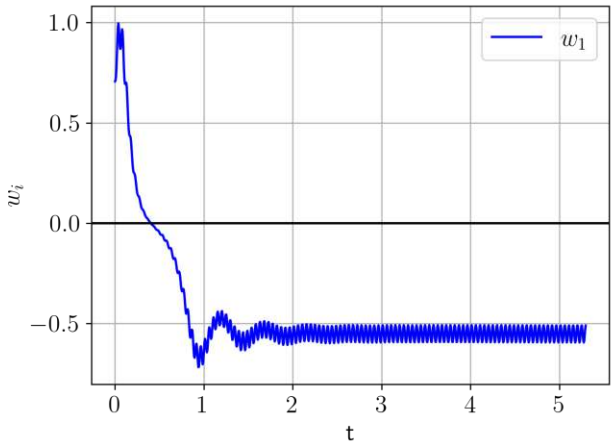


**Figure 5.1:** Single Piezo Tone with $f_p = 21.0$ and $N_0^{(p)} = 0.98$: Trajectory of Maximum Mode 1 Deflection over Time

This trajectory indicates that such a tone causes snap-through at approximately $t = 0.5$, when the maximum mode 1 deflection $w_1$ first reaches zero. Ultimately, the plate deflection then reaches a oscillatory behavior near its negative stable deflection

point, with a frequency of oscillation that matches the piezo frequency $f_p = 21.0$. In this overall behavior, two regions of interest become immediately apparent, the first being the time that leads to snap-through initiation, and the second being the post snap behavior. Since we are primarily interested in snap-through time, we will focus on the first region going forward.

Although the trajectory of the maximum modal deflection of the plate over time is insightful, to better understand the behavior of the system for a wide variety of applied piezo tones, it became useful to plot the initial snap time of the system on a 2D map of piezo tones of different frequencies and amplitudes as defined by Equation 5.1.

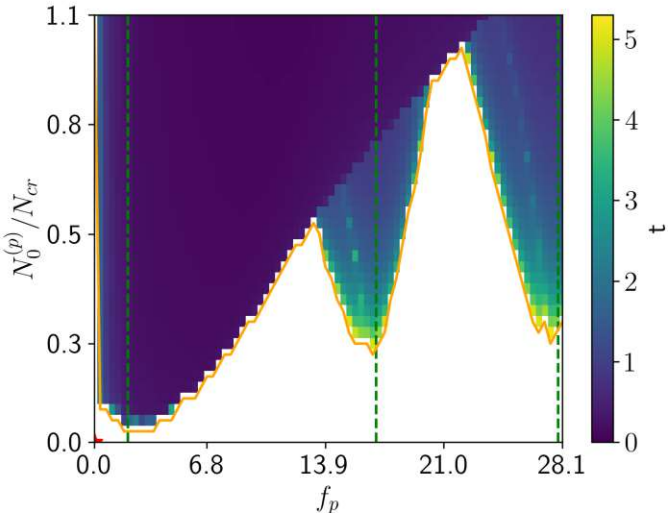


**Figure 5.2:** Single Piezo Tone: Map of Initial Snap Times of Mode 1

Figure 5.2 illustrates this 2D map for single piezo tones with some frequency $f_p \in (0.01, 28.11)$ and $N_0^{(p)} \in (0, 1.1)$. These bounds in particular were chosen so that these results could be directly compared with the results of a previous work, which they very closely match [6]. Each ppint represents a simulation with a different piezo tone, and the color of the pixel represents the time until the system had the first snap-through. If the points is white (lack of color points), then no snap-through occurred during the entire simulation time duration. The orange line

represents the boundary between the snap and no-snap regions for this map in particular, and serves as a useful reference for comparing this map to other maps with different conditions.

The three vertical dashed green lines then mark the eigenfrequencies of each mode of the system. These eigenfrequencies line up with the bottom of each of the three "tongue" formations in the map. The eigenfrequency $f_{eigen,1} = 1.99581$ of the first mode marks the tongue on the left, the eigenfrequency $f_{eigen,2,3} = 16.69734$ of the second and third modes marks the tongue on the in middle, and then the eigenfrequency $f_{eigen,4} = 27.49158$ of the fourth mode marks the tongue on the right.

To better understand how each mode contributes to the overall deflection behavior of the plate, we can define the participation factor for each mode to be

$$\lambda_i = \frac{\langle |q_i(t)| \rangle}{q_1(0)} \tag{5.5}$$

where $\langle |q_i(t)| \rangle$ is the absolute value of the deflection of the mode averaged over time. Accordingly, this is a measure of how much each mode is deflecting on average compared to the initial deflection $q_1(0)$ of mode 1 .

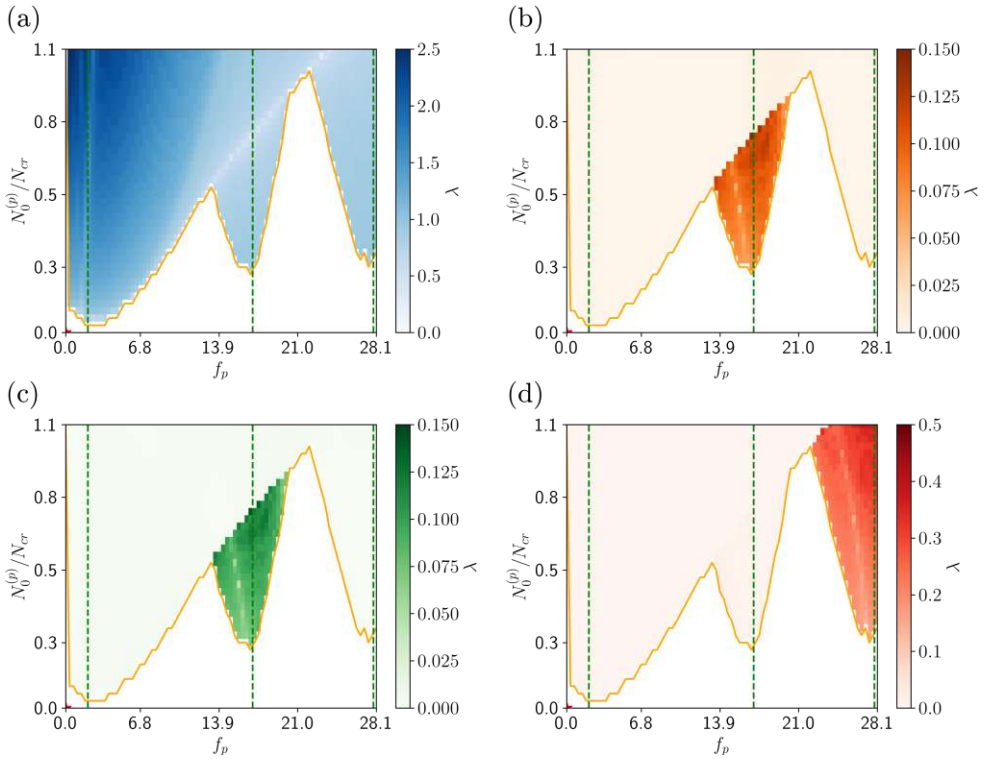


**Figure 5.3:** Single Piezo Tone: Maps of Modal Participation Factor. Mode 1 (a), Mode 2 (b), Mode 3 (c), and Mode 4 (d).

By plotting the participation of each mode over the same domain as 5.2, we then obtain Figure 5.3. These plots clearly illustrate that mode 1 dominates the behavior for the left tongue, modes 2/3 for the middle, and mode 4 for the right. This matches the observed eigenfrequency correlation. One aspect to note is that for these simulations, the event detection system described in 3.5 was used, so if a snap-through occurred, then the time series collected for that simulation stopped at the snap time. So these modal participation factors only take into account the deflection behavior up to the time of snap-through, as we were primarily interested in observing which modes contribute most to the initiation of snap-through.

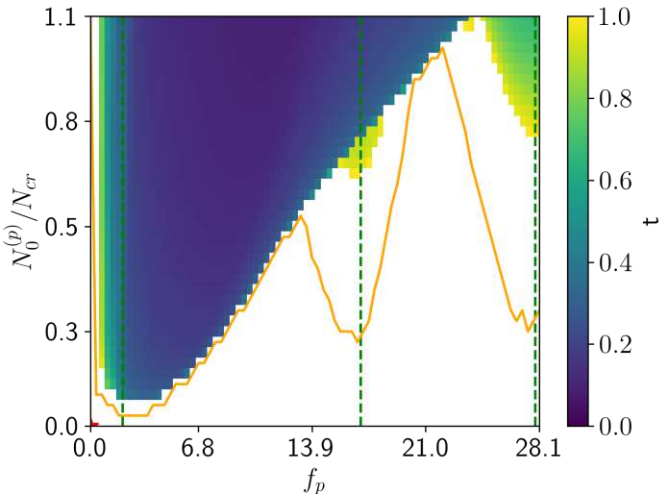


**Figure 5.4:** Single Piezo Tone: Map of Small Initial Snap Times ($t \leq 1$)

Figure 5.4 is based on the same data as Figure 5.2, but only snap-throughs at the smaller time regime of $t \leq 1$ are displayed. It is evident that the tongues for modes 2/3 and mode 4 almost vanish, while the mode 1 tongue is mostly retained. This suggests that, for these particular conditions, mode 1 is the main contributor to a rapid snap-through, while the other modes may contribute to slower snap-through times.

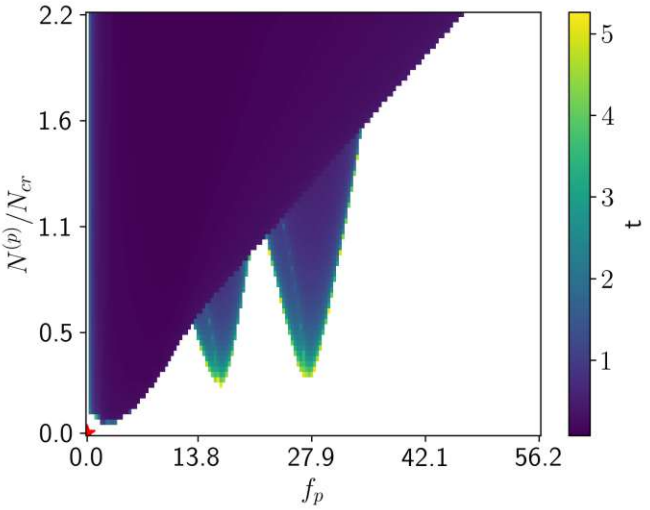


**Figure 5.5:** Single Piezo Tone: Map of Initial Snap Times for a Larger Domain

Figure 5.5 extends the simulation domain from Figure 5.2 to double the possible frequencies and double the possible amplitudes. Now, the simulations are shown for the application of single piezo tones with some frequency $f_p \in (0.01, 56.22)$ and $N_0^{(p)} \in (0, 2.2)$. For frequencies past the tongue of mode 4 ($f \gtrapprox 35$), no further tongues appear, and larger and larger amplitudes are needed for those frequencies of piezo tones to induce snap-through, as an approximately linear boundary of the mode 1 tongue forms to separate itself from the no snap region. Due to the lack of additional features and the high amplitude needed to induce snap-through, this higher frequency piezo regime appeared less promising for finding new ways to efficiently induce snap-through than the original domain from Figure 5.2. Thus we focused on the domain of Figure 5.2 as a reference for comparison going forward.

## 5.3 Eigenfrequency-Matched Dual Tones

With the single tone case examined, the many possibilities with dual tones provided a method for examining the effects of more complex tones, while still being able to compare to the single tone case. The first case examined was the case where the frequency one of the two tones was fixed at one of the eigenfrequencies of the modes, at a variety of amplitudes. The other tone was then varied in frequency and amplitude to produce maps (varied from one simulation to another; the

frequency/amplitude were constant within each simulation). The results of these cases are shown in Figure 5.6.

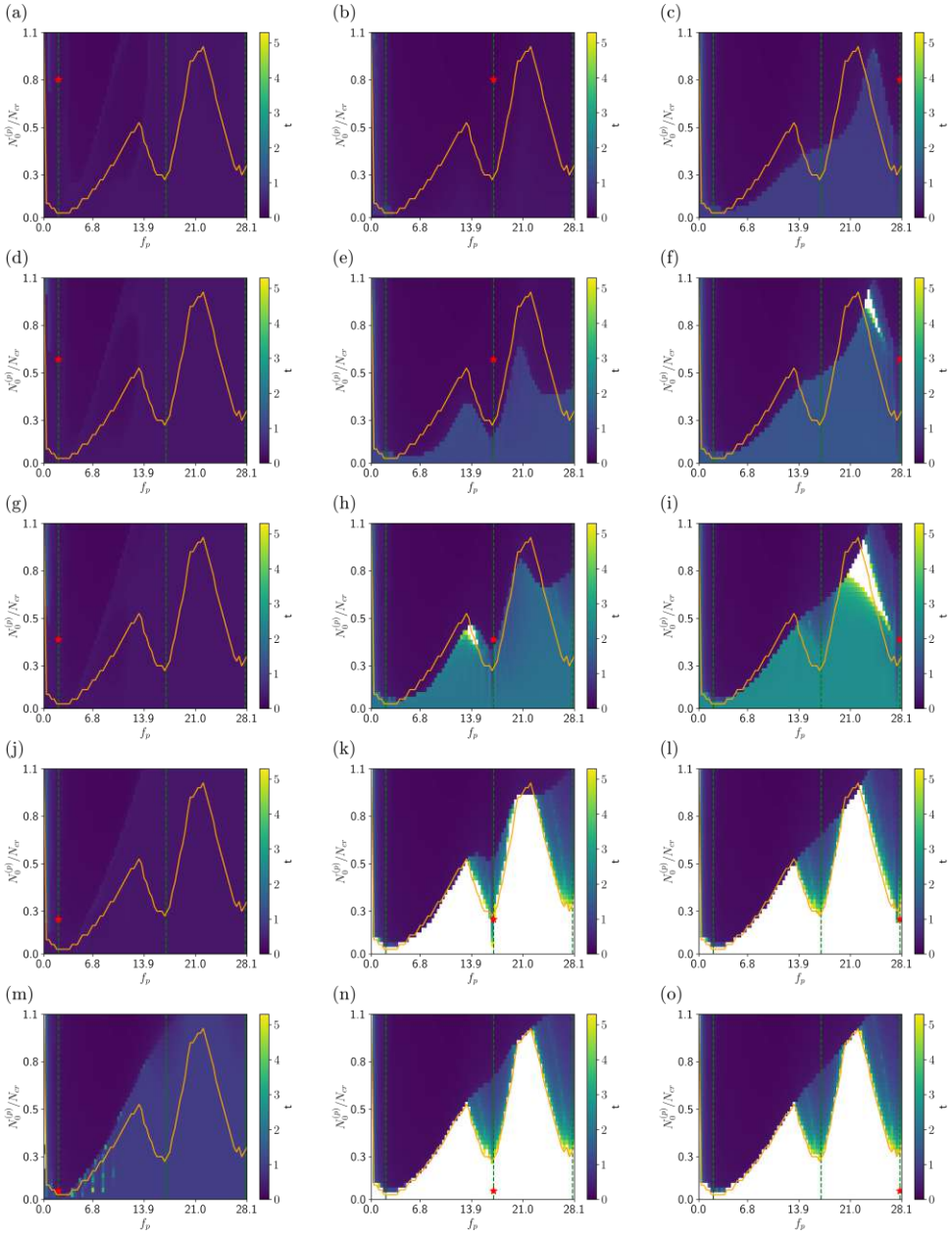


**Figure 5.6:** Eigenfrequency-Matched Fixed Tones: Dual Tone Maps of Initial Snap Times

In Figure 5.6, 15 sets of maps are shown. Each has a different fixed tone corre-

sponding to the red star marked on each plot. The first column from the left has fixed tones with frequencies matching the mode 1 eigenfrequency, whereas the second column matches that of mode 2/3, and the third column matches mode 4. Each row then shows a different amplitude of this fixed tone, from $N_{0,f}^{(p)} = 0.05$ at the bottom to $N_{0,f}^{(p)} = 0.8$ at the top. Figure 5.7 shows the positions of the fixed tones annotated on the single-tone map of Figure 5.2.

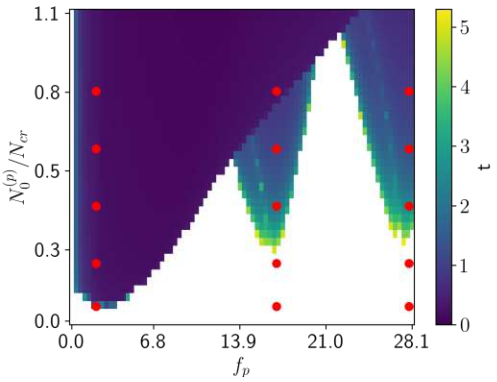


**Figure 5.7:** Eigenfrequency-Matched Fixed Tones of Interest Annotated on Single-Tone Map

From Figure 5.6, we observed that as the amplitude of the fixed tone increases, generally a greater proportion of the map exhibits snap-through behavior, corresponding to more combinations of tones being able to induce snap-through within the simulation time. And once amplitude exceeds the values indicated by the orange border (the snap boundary from the single tone map), most dual tones begin to exhibit snap-through at some point, as illustrating by the reduction of the white regions. However, some "holes" were observed to form, in particular between the 0.2 to 0.4 amplitudes of fixed tones at the mode 2/3 (plot (k) to plot (h)) and mode 4 eigenfrequencies (plot (l) to plot (i)), where a pocket of non-snap-inducing tones (in white) are surrounded by snap-inducing tones (non-white). This is surprising because there a tones with lower amplitudes than the holes that induce snap-through. Thus, increasing the amplitude does not guarantee that snap-through will occur or continue to occur.

Furthermore, for plot (m) where the fixed portion of the tone is ($f_{p,f} = f_{eigen,1}, N_{0,f}^{(p)} = 0.05$) , some curious vertical lines with higher snap time results appeared. This is

examined more closely in Section 5.5.

To better understand the relative effect on snap-through time by the application of these additional fixed tones, we can plot the difference in snap-through time between the single tone case and the dual tone case. This is shown in Figure 5.8. This figure shows that for the fixed tone at the eigenfrequency of mode 1, the snap-through time is reduced for a large range of frequencies and amplitudes of the other tone. This is especially true for the lower frequency range of the other tone. For the fixed tones at the eigenfrequency of mode 2/3 or 4, the snap-through time is reduced for a large range of frequencies and amplitudes of the other tone, but the effect is not as strong as for the mode 1 case.

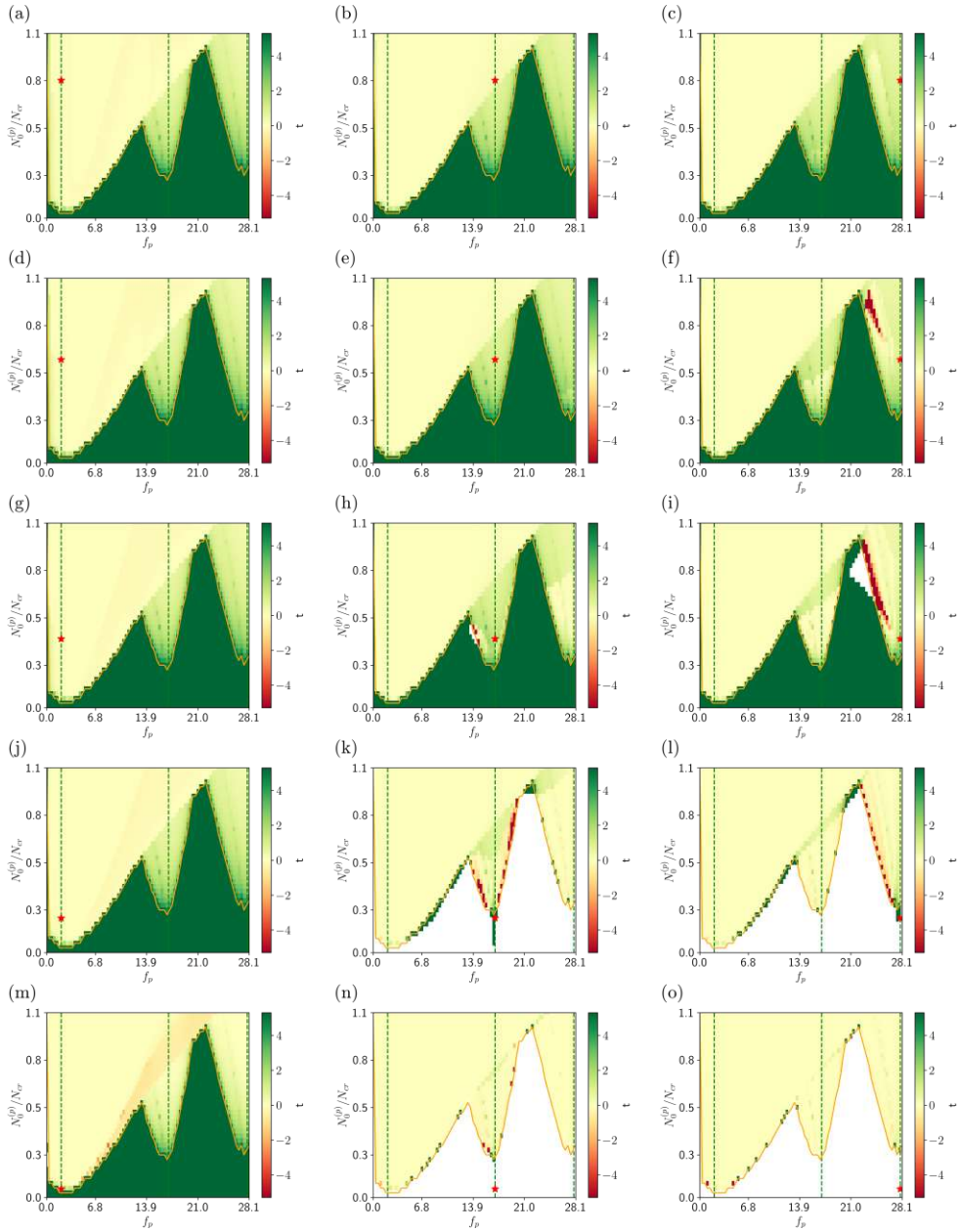


**Figure 5.8:** Eigenfrequency-Matched Fixed Tones: Dual Tone Maps of Difference in Snap Times from Single Tones

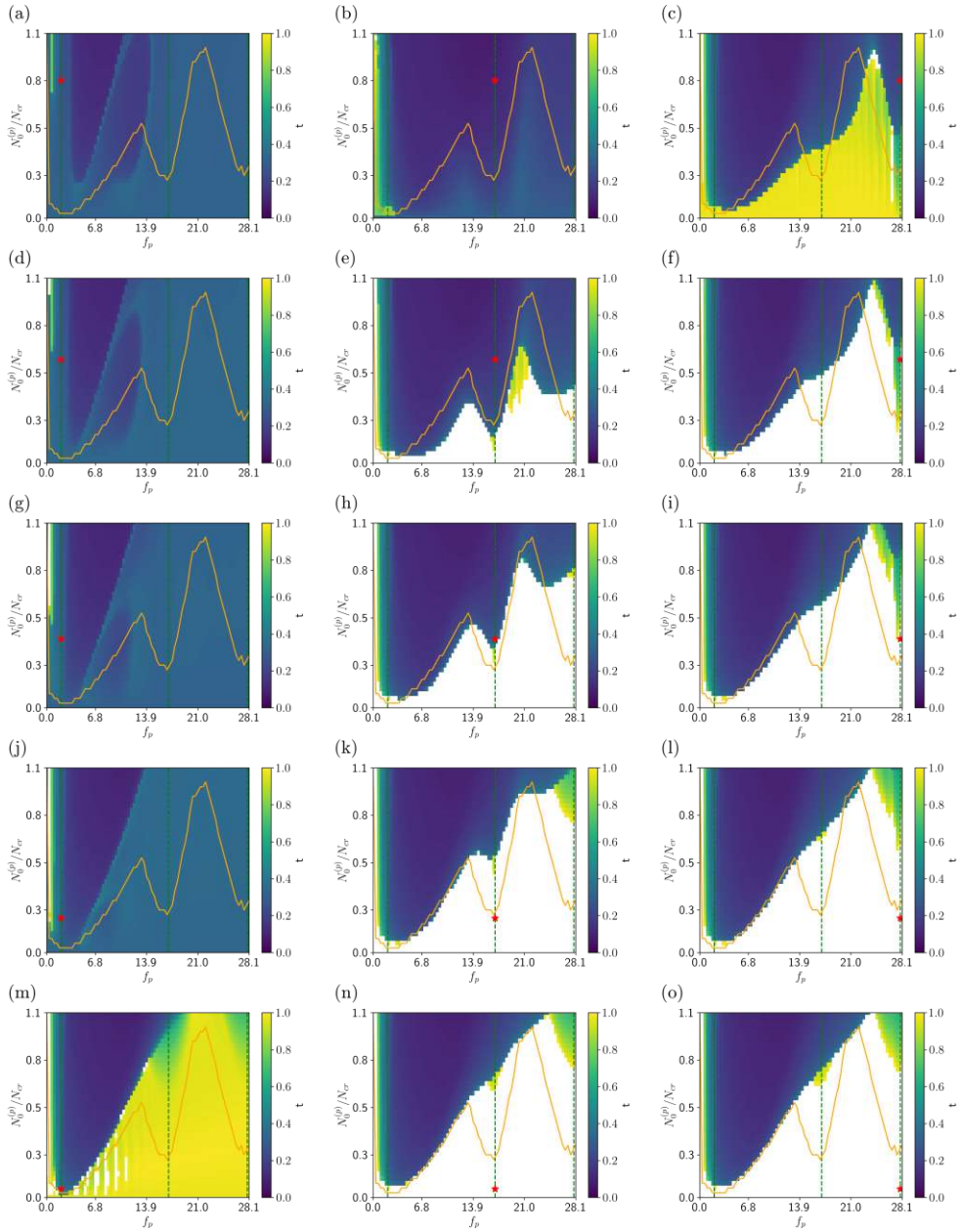


**Figure 5.9:** Eigenfrequency-Matched Fixed Tones: Dual Tone Maps of Small Initial Snap Times $t \leq 1$

Figure 5.9 shows the snap times $t \leq 1$ instead of the full simulation time. In doing so, we see more refined detail on the vertical line formations in plots (m) and (c).

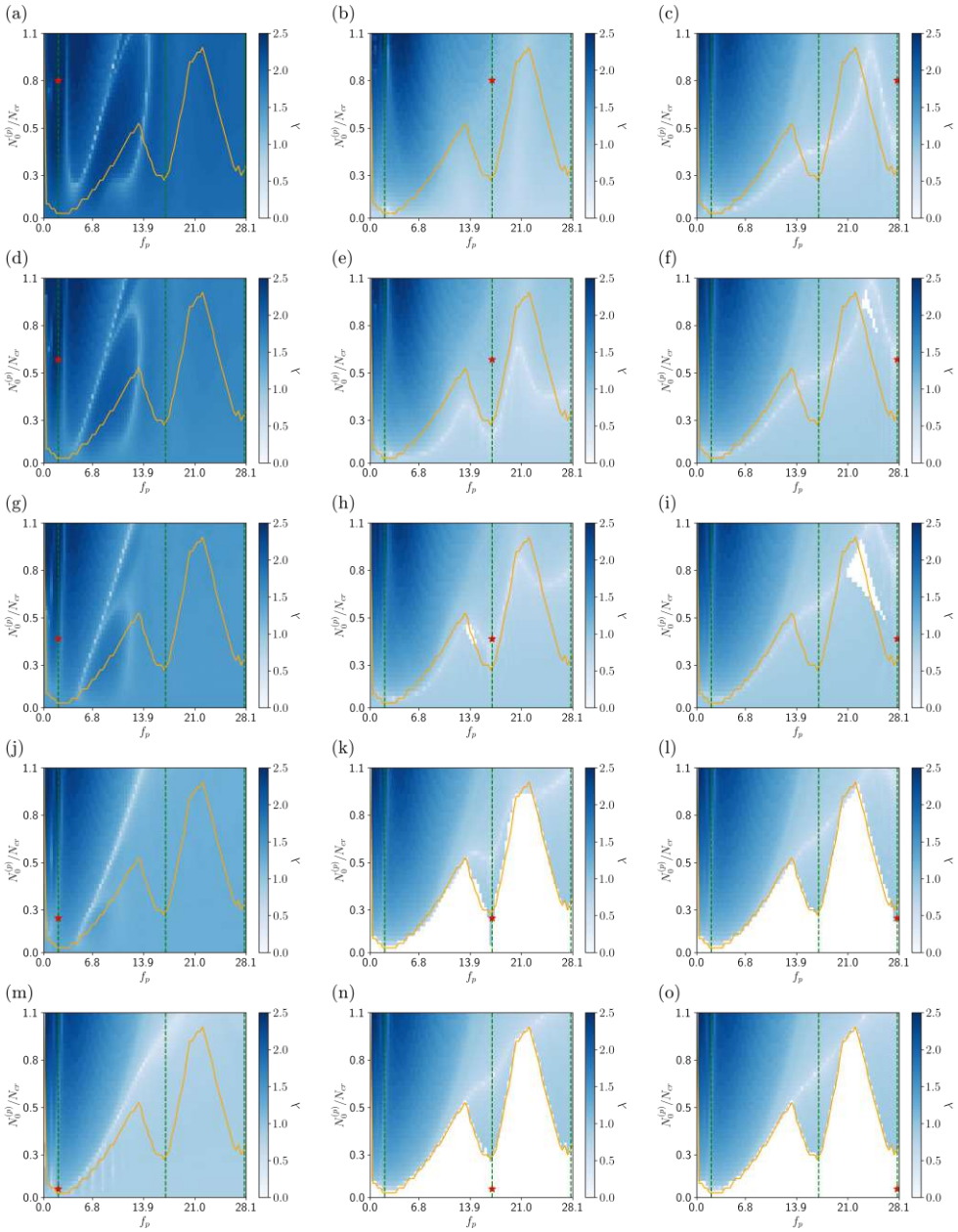


**Figure 5.10:** Eigenfrequency-Matched Fixed Tones: Dual Tone Map of Mode 1 Participation Factor

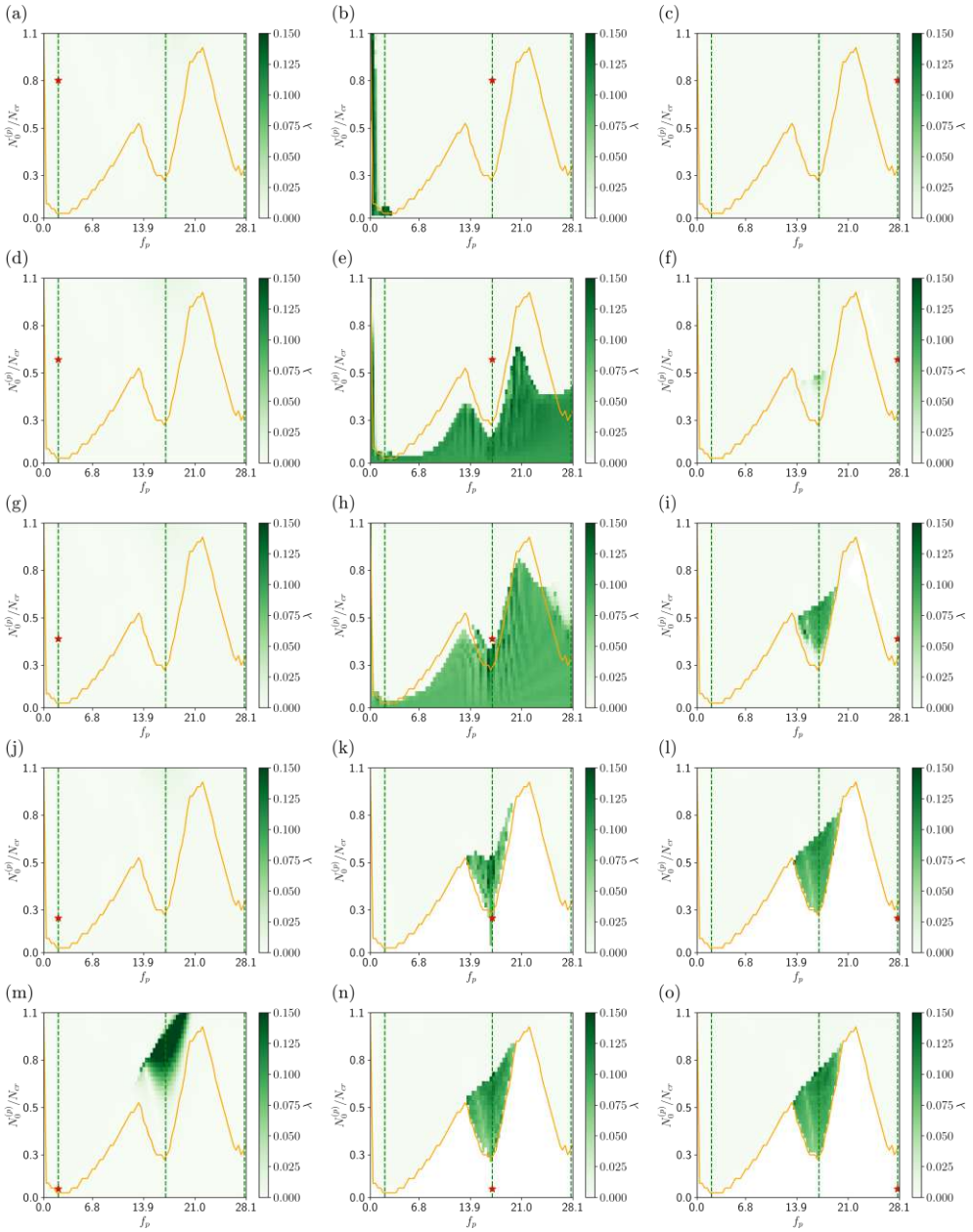


**Figure 5.11:** Eigenfrequency-Matched Fixed Tones: Dual Tone Map of Mode 2/3 Participation Factor

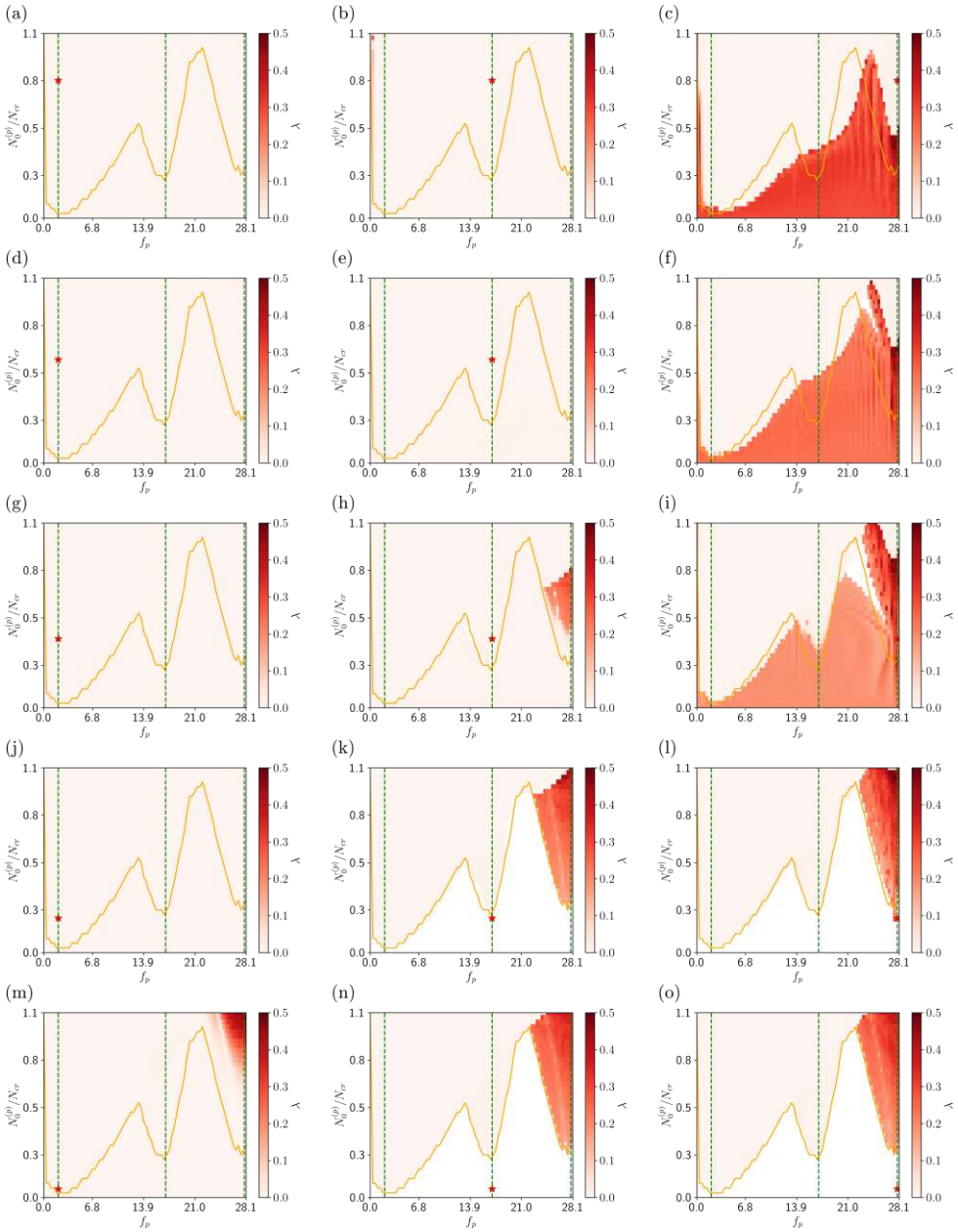


**Figure 5.12:** Eigenfrequency-Matched Fixed Tones: Dual Tone Map of Mode 4 Participation Factor

Figures 5.10, 5.11, and 5.12 all show the participation factors for modes 1, 2/3, and 4 respectively. Modes 2/3 are shown together as one set of plots because these two modes exhibit the same participation factors. Here, we can see that for fixed tones

outside of the tongues, the participation of each mode mostly remains within its respective tongue region. However, once the fixed tone is with the tongue regions, the corresponding modal participation factor is amplified and "spills" onto other portions of the maps, indicating that this modes are playing a significant role in the deflection behavior exhibited by these particular dual tones.

## 5.4 Dual Tone Snap-Time Modulation

When looking at individual combinations of dual tones from the previous maps, we see four especially intriguing possibilities of behavior. One, for some combinations of fixed and variable tone, the snap-through time is reduced compared to the times for each tone alone. Two, there are cases where snap now occurs within the time frame of the simulation, whereas it did not occur for each tone alone. Three, there are cases where snap-through time is increased compared to each tone alone. Four, there are cases where snap-through does not occur within the time frame of the simulation, whereas it did occur for each tone alone. The following figures highlight examples of each of these four cases. Each of these figures plots the position of the two components of the dual tone on the single tone map for reference (left), the maximum deflection over time as a response to each tone and their combination (middle), and the value of the combined dual tone over time (right).

### 5.4.1 Faster Snap-Through

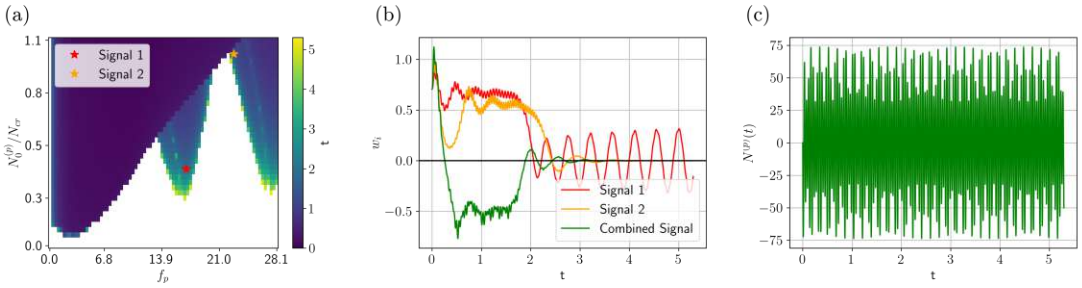


**Figure 5.13:** Dual Tone: Faster Snap-Through

Figure 5.13 demonstrates an example of snap-through becoming faster through the combination of tones each with different frequencies and amplitudes. Tone 1 ($f_p = f_{eigen,1}, N_0^{(p)} = 0.4$) snaps at approximately $t = 2$ and Tone 2 ($f_p = 22.5, N_0^{(p)} = 1.0$)

snaps at approximately $t = 2.5$, but their combination snaps at just less than $t = 0.5$.

### 5.4.2 Emergent Snap-Through

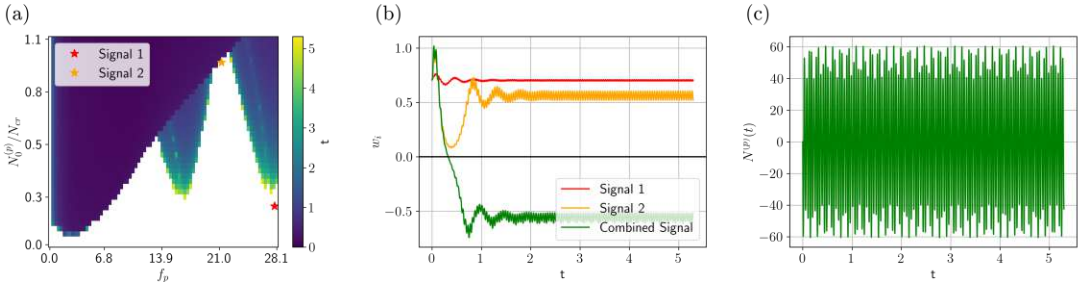


**Figure 5.14:** Dual Tone: Emergent Snap-Through

Figure 5.14 illustrates an example of emergent snap-through occurring through the combination of tones. Both Tone 1 ($f_p = f_{eigen,4}, N_0^{(p)} = 0.2$) and Tone 2 ($f_p = 21, N_0^{(p)} = 0.95$) don't fully snap-through within the simulation time, and instead oscillate near their positive static equilibrium. However, their combination snaps at just less than $t = 0.5$, and then settles in an oscillatory state near the negative static equilibrium.

### 5.4.3 Slower Snap-Through

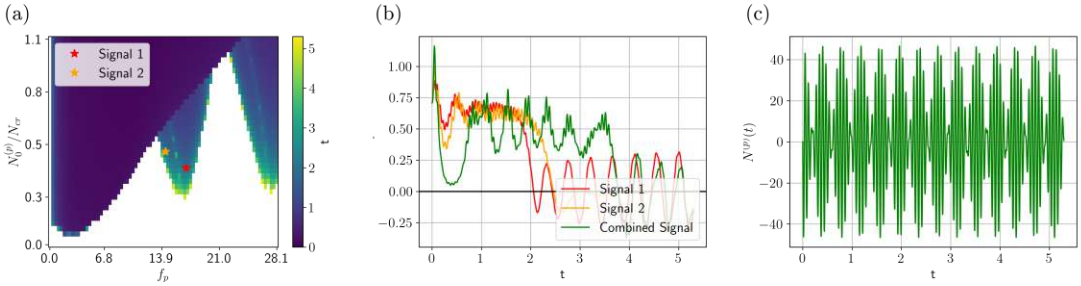


**Figure 5.15:** Dual Tone: Slower Snap-Through

Figure 5.15 , however, demonstrates an example of snap-through becoming slower through the combination of tones. Tone 1 ($f_p = f_{eigen,2,3}, N_0^{(p)} = 0.4$) snaps at approximately $t = 2$ and Tone 2 ($f_p = 14.15, N_0^{(p)} = 0.485$) snaps at approximately $t = 2.5$ However, their combination snaps at about $t = 4$. Here, the tones effects

on the deflection seem to interfere with each other and cause this extended time until the first snap-through.

### 5.4.4 No Snap-Through

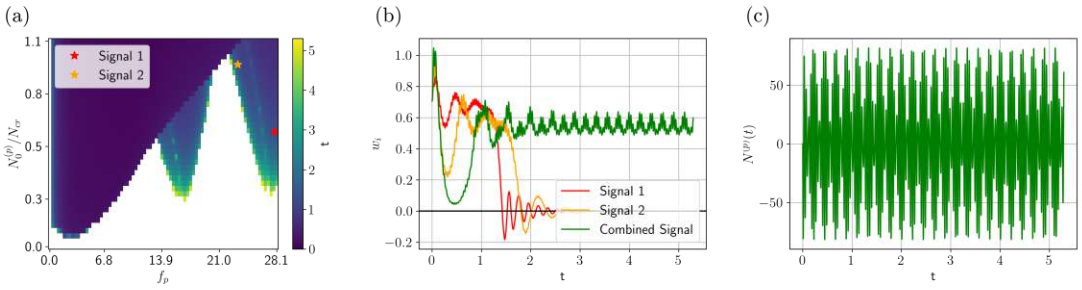


**Figure 5.16:** Dual Tone: No Snap-Through

In contrast to the previous cases, Figure 5.16 demonstrates an example of snap-through being completely prevented during the simulation time through the combination of tones. Tone 1 ($f_p = f_{eigen,2,3}, N_0^{(p)} = 0.6$) snaps at approximately $t = 1.5$ and Tone 2 ($f_p = 23, N_0^{(p)} = 0.95$) snaps at approximately $t = 1.75$ However, their combination exhibits no snap-through at all, although it does cause the deflection to become quite close to doing so at about $t = 0.5$

## 5.5 Mode 1 Eigenfrequency Dual Tone Closeup

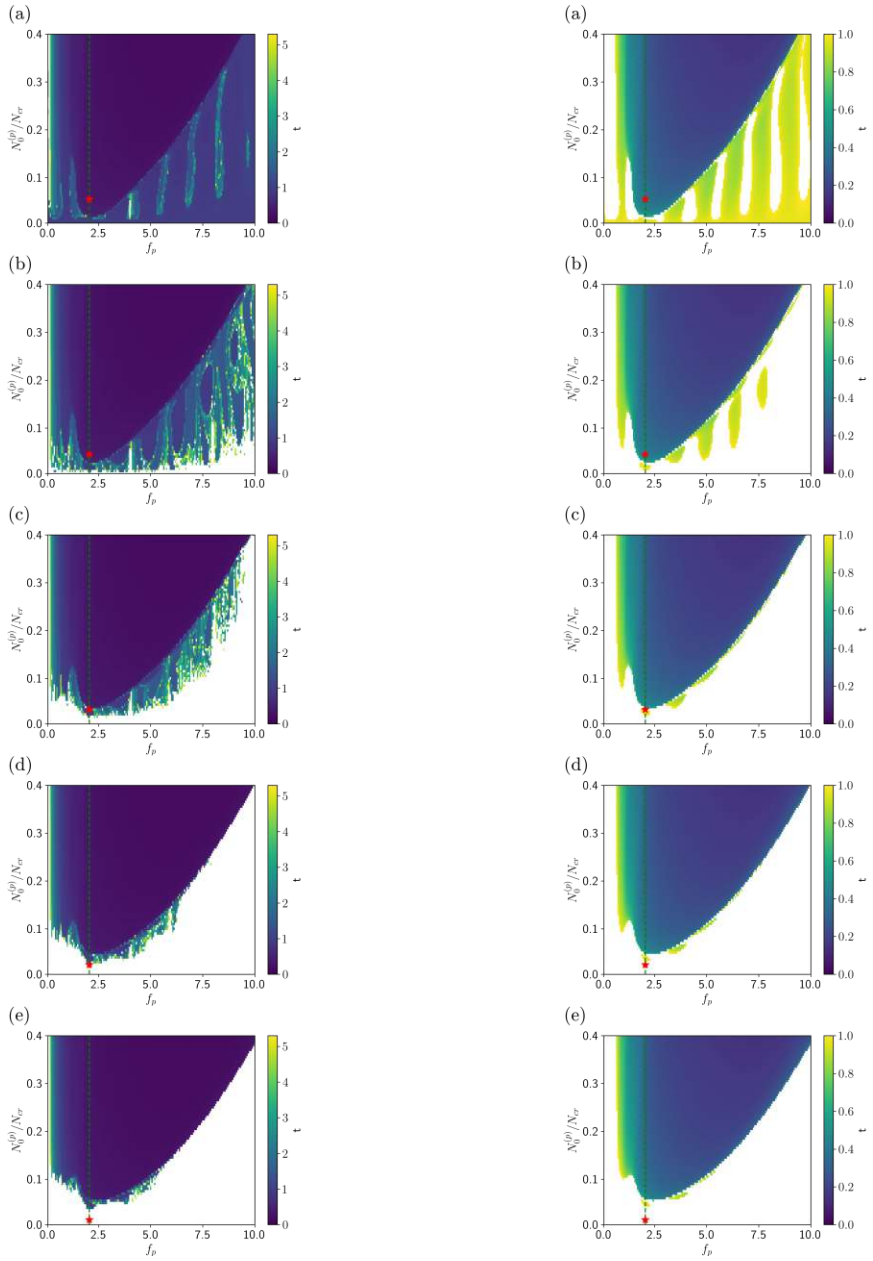


**(a)** Initial Snap Time **(b)** Initial Small Snap Times $t \leq 1$

**Figure 5.17:** Dual Tones with Fixed Tones Matching $f_{eigen,1}$: Maps of Snap Times for Low Frequencies/Amplitudes

Figure 5.17 depicts a closeup of the dual tone plots with the fixed tone frequency matching $f_{eigen,1}$, and with $N_{0,f}^{(p)} \in (0.01, 0.05)$. The bounds of the map have between constrains to the lower frequencies of $f_{p,v} \in (0, 10)$ and lower amplitudes of $N_{0,f}^{(p)} \in (0.0, 0.4)$, in order to observe finer details in this region. In particular, the roughly vertical regions of longer initial snap time that form as the fixed amplitude to 0.05 is increased is of particular interest. Furthermore, these regions appear to exhibit fairly periodic behavior relative to frequency. And especially at the amplitude of 0.04, fractal-like formations become apparent.

## 5.6 Non-Eigenfrequency-Matched Dual Tone

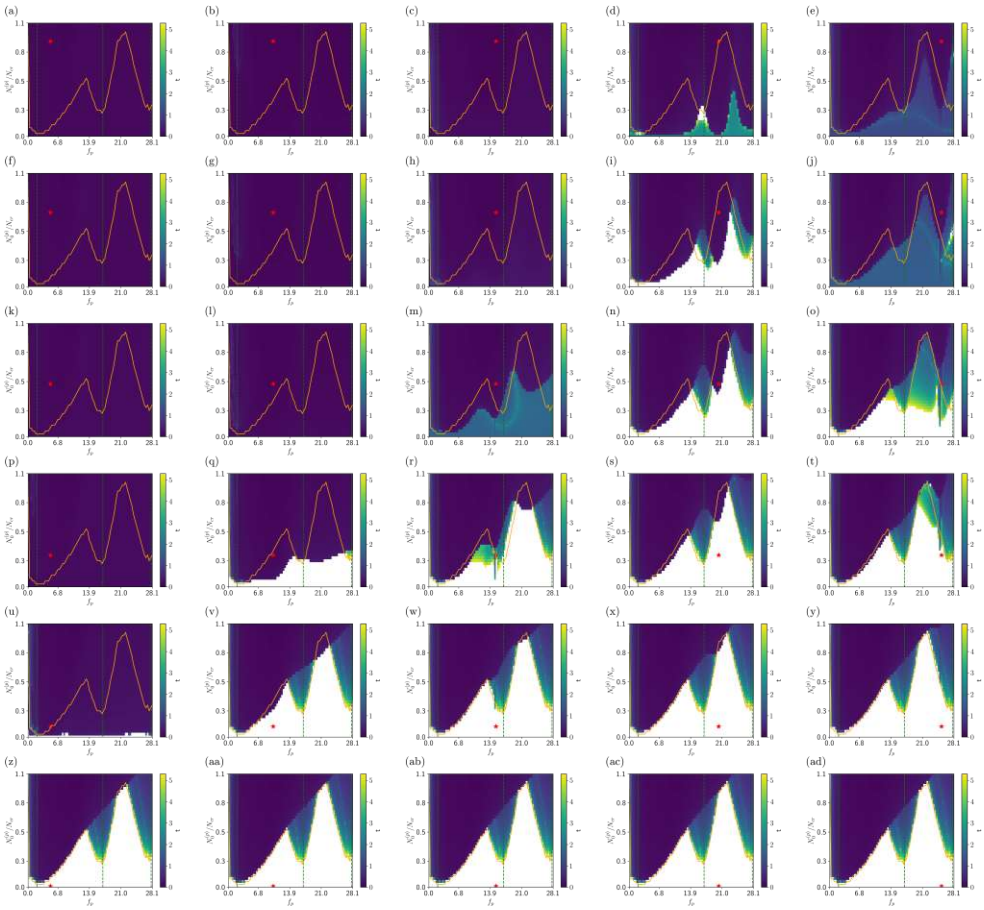

**Figure 5.18:** Non-Eigenfrequency-Matched Fixed Tones: Map of Initial Snap Times of Dual Tone

Figure 5.18 depicts plots of maps where the fixed portion of the dual tone had frequencies not at the eigenfrequencies of the system, but instead at $f_p \in \{5, 10, 15, 20, 25\}$. Figure 5.19 shows the positions of the fixed tones annotated on the single-tone map of Figure 5.2.

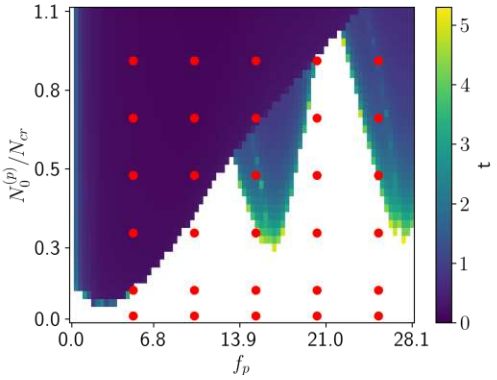


**Figure 5.19:** Non-Eigenfrequency-Matched Fixed Tones of Interest Annotated on Single-Tone Map

Many of the plots depict patterns similar to those observed from the case of eigenfrequency matching, but some notable differences emerge. For the column of plot (d), another tongue-like formation appears to emerge as the fixed amplitude increases, with this formation being centered around the fixed frequency.

## 5.7 Phase-Shifted Dual Tone

To study how a phase difference between the two components of a dual tone would affect the resulting snap-through time, each of the phases $\varphi \in \left\{\frac{\pi}{4}, \frac{\pi}{2}, \pi\right\}$ were individually incorporated into the fixed tone, and then the 2d maps were made once again for each case, as illustrated in Figures 5.20, 5.21, 5.22

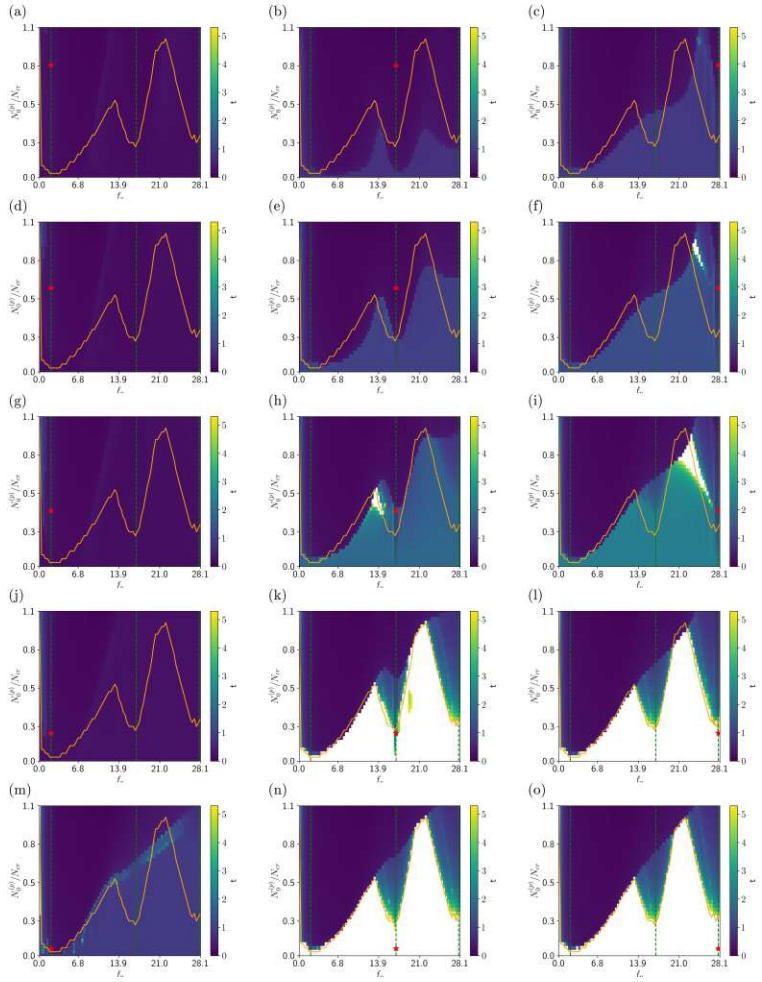

**Figure 5.20:** Phase Shift = $\frac{\pi}{4}$: Maps of Dual Tone Initial Snap Times

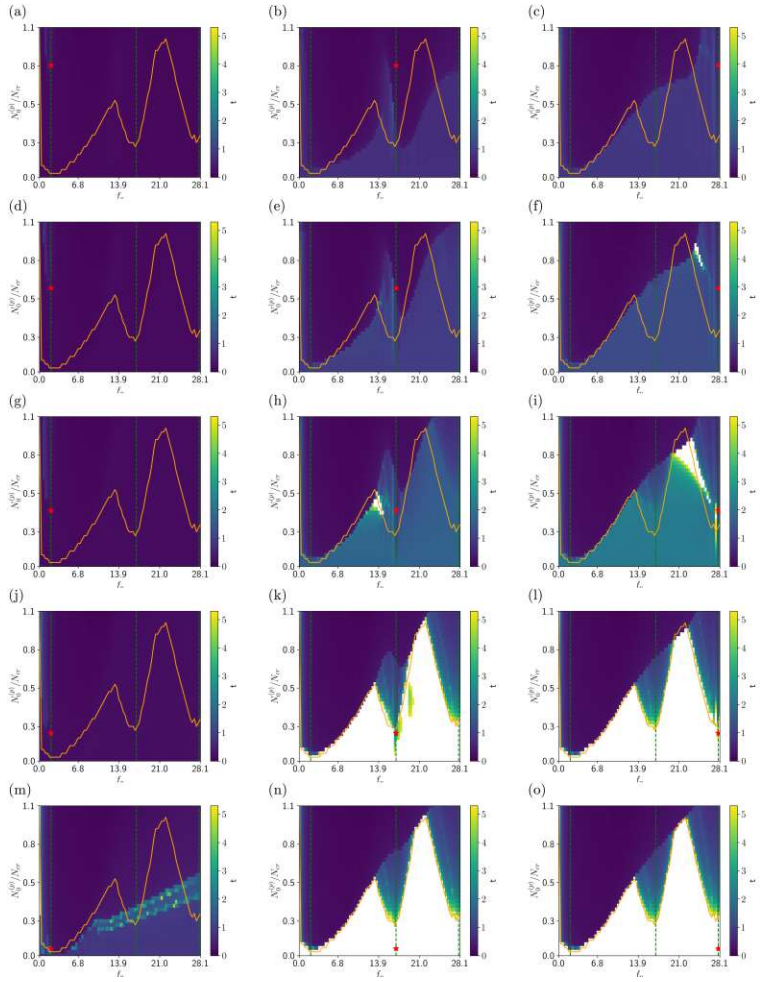

**Figure 5.21:** Phase Shift = $\frac{\pi}{2}$: Maps of Dual Tone Initial Snap Times

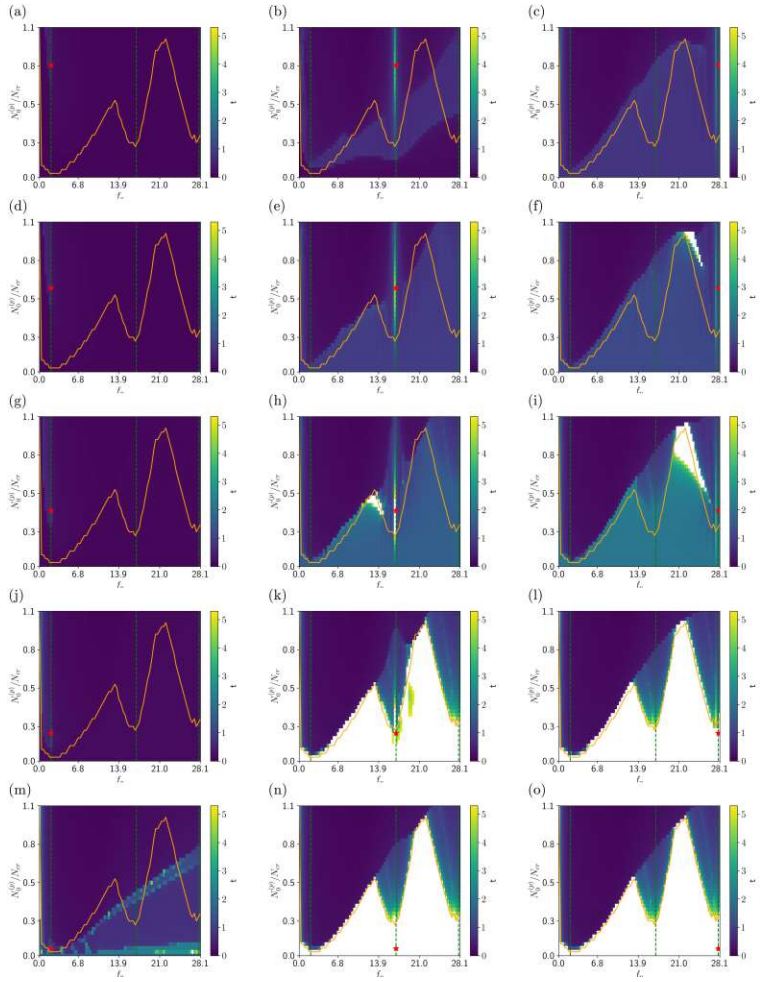

**Figure 5.22:** Phase Shift = $\pi$: Maps of Dual Tone Initial Snap Times

One of the most intriguing features of these plots appears in Figure 5.22 for a case of a phase shift of $\pi$. For the $f_{p,f} = f_{eigen,2,3}$, a very narrow vertical line appears at the eigenfrequency, and along this line the snap-through times are rather long or even don't occur at all. This appears to be the result of the phase shift causing each half of the tone to nearly cancel the other out when their frequencies match rather precisely. Comparing these plots to the case of no-phase-shift as was the case with Figure 5.6, we see the greatest differences in the snap-time profile of the plot when the two frequencies of the dual tone are closer in value.

## 5.8 Damping-Dependence

To study how the snap-through time of the dual tones would change as the damping ratio was altered, simulations were run for three additional damping ratios in additional to the normal setting. These include damping ratios of $0.5\kappa$, $0.25\kappa$, and $2\kappa$.

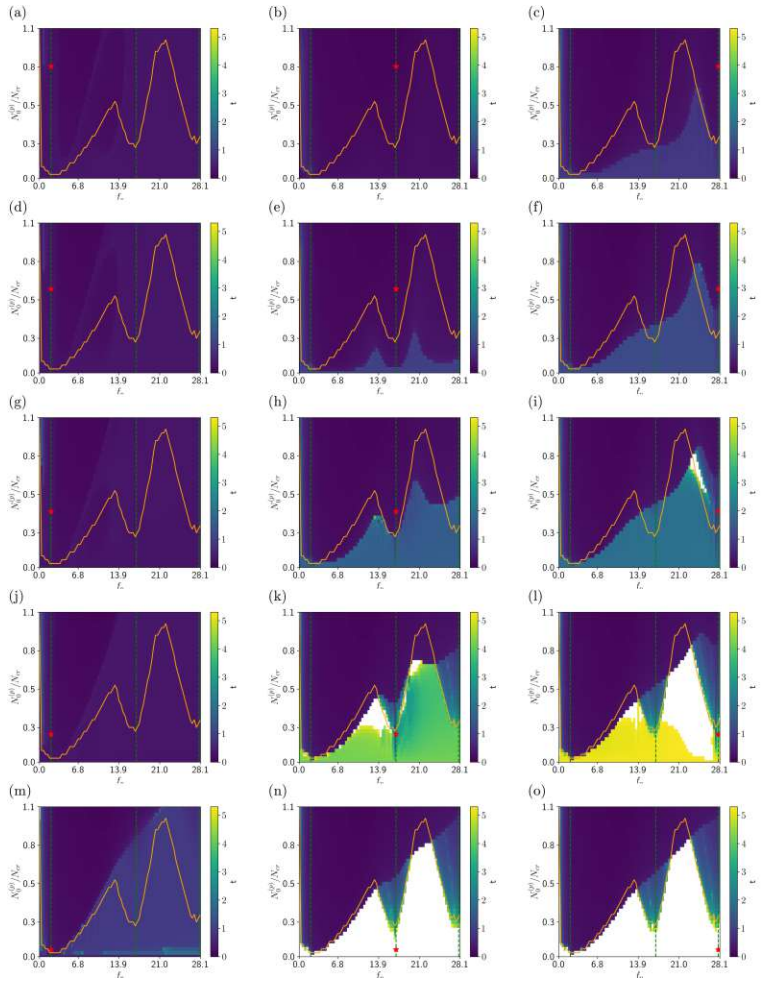

**Figure 5.23:** Damping = $0.5\kappa$: Maps of Dual Tone Initial Snap Times

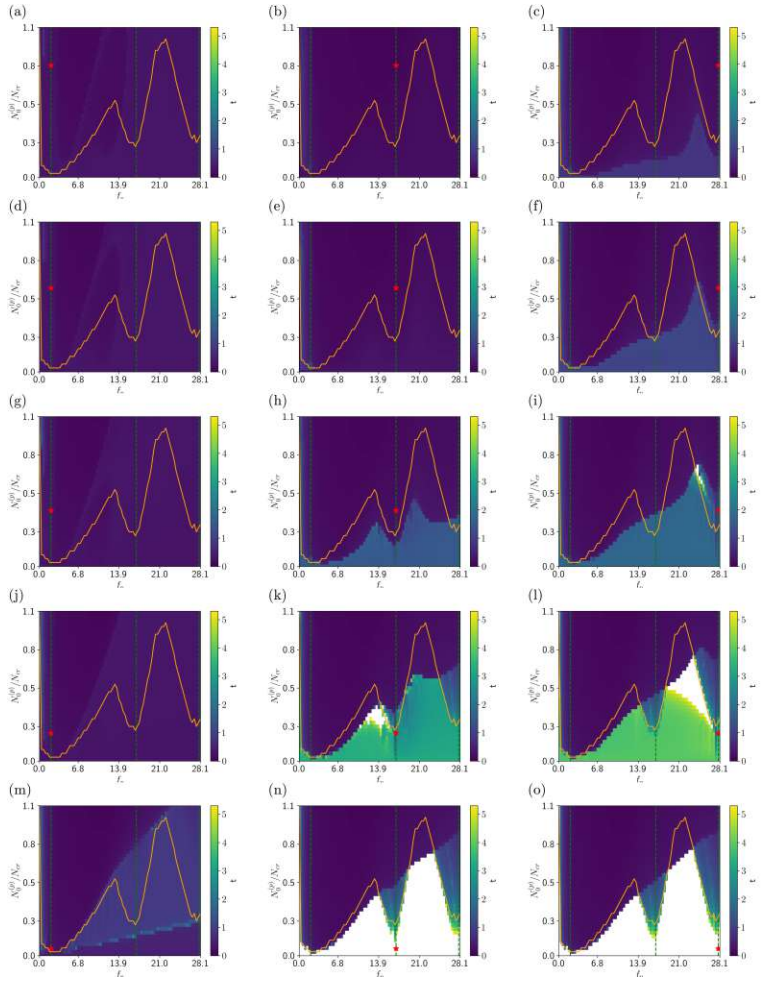

**Figure 5.24:** Damping = $0.25\kappa$: Maps of Dual Tone Initial Snap Times

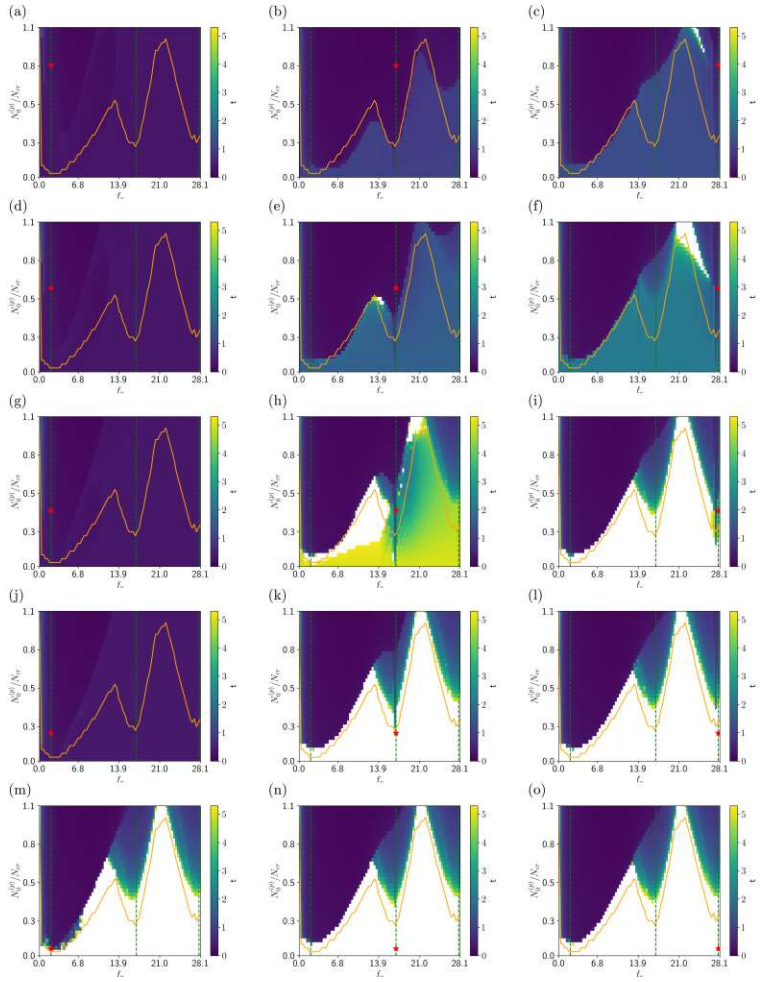

**Figure 5.25:** Damping = $2\kappa$: Maps of Dual Tone Initial Snap Times

From Figures 5.23, 5.24, and 5.25 we can see that as the damping increases, most of the plots appear to shift upwards, indicating that a higher amplitude tone is needed to overcome this higher damping and induce snap for at a given frequency. Similarly, as the damping decreases, most of the plots appear to shift downwards, indicating that the amplitude no longer needs to be as high to induce snap for at a given frequency. For a damping of $0.25\kappa$ in particular, the plot (m) where the fixed portion of tone has ($f_{p,f} = f_{eigen,1}, N_{0,f}^{(p)} = 0.05$) exhibits a very short snap time across all of the low amplitudes in that domain.

# CHAPTER 6

# Conclusion

This study set out to explore the effect of piezoelectric excitations of dual-frequency tones,on snap-through behavior within the microplate system. The single tone case provided a fundamental understanding which served as a basis for more complex dual tone simulations. Our results underscore the intricate relationships between tone combinations and the resulting snap-through behavior. Specifically, there were instances where combinations of dual tones induced more rapid snap-through times, delayed snap-through, enabled emergent snap-through, or even prevented snap-through entirely. Understanding how to cause snap-through quickly is particularly important, since this makes the snap-through more responsive to input signals, which may be very useful for real-world devices. Furthermore, a faster snap-through may require less energy overall since the input signal for the piezoelectric excitation (such as a voltage signal) could be run for a shorter amount of time. Thus, the variety of ways in which snap-through time can be altered by dual tones illustrates which tones are more promising (quicker or emergent snap), or better to avoid (slower or no snap).

A major observation is that an increase in the amplitude of a fixed tone does not necessarily equate to consistent snap-through occurrence. There are scenarios, particularly between certain amplitude ranges of fixed tones at eigenfrequencies, where increasing the amplitude led to pockets of non-snap-inducing excitation parameters. This goes against the idea that higher amplitudes more readily instigate snap-through. Instead, a more nuanced approach is needed to calibrate

the amplitude to avoid these pockets.

When looking into the phase-shifted dual tones, the introduction of a phase difference had more of an effect on the snap-through time when the two frequencies of the dual tone were closer in value, since this could cause either constructive or destructive interference of the overall tone, and result in a faster or slower snap-through time. Thus, if the phase difference were to be hard to control for some real-world application, then it may be more suitable to use dual tones with significantly different frequencies. However, if one desires to use similar-frequency dual tones, then care is needed in order to select the right phase difference to cause constructive interference of the overall tone in order to quickly induce snap-through.

Furthermore, the damping-shifted dual tones displayed expected trends: increased damping required higher amplitude tones to achieve snap-through, while reduced damping showed the opposite. This finding has significant implications for the design of systems where control over snap-through behavior is crucial. The damping must be accurately understood in order to predict which amplitude of tone is necessary to induce snap-through. This is important for energy savings, since by minimizing the amplitude while still quickly snap-through, one needs less energy to maintain the tone (via a voltage signal for instance).

In essence, this research has made it evident that the simple act of combining two tones in a system can lead to a myriad of complex outcomes, especially in terms of increasing or decreasing the snap-through time. Understanding these behaviors, particularly in the context of snap-through dynamics, provides a pathway for more controlled, efficient, and targeted applications in real-world scenarios where rapid snap-through is crucial. Whether in the design of sound-generating devices, mechanical switches, or other applications, the findings of this study could help support innovative approaches that take advantage of these intricate dual-tone interactions. Future approaches to expand upon this study could include examining microplate shapes other that a square shape. This could include a circular shape or even a ring shape similar to designs for MEMS speakers [4].

# List of Figures

# List of Tables

# List of Algorithms

# Bibliography


[1] Xianhao Le, Qiongfeng Shi, Philippe Vachon, Eldwin J. Ng, and Chengkuo Lee. Piezoelectric MEMS—evolution from sensing technology to diversified applications in the 5G/Internet of Things (IoT) era. *Journal of Micromechanics and Microengineering*, 32(1):014005, December 2021. Publisher: IOP Publishing.

[2] Abdullah Saleh Algamili, Mohd Haris Md. Khir, John Ojur Dennis, Abdelaziz Yousif Ahmed, Sami Sultan Alabsi, Saeed Salem Ba Hashwan, and Mohammed M. Junaid. A Review of Actuation and Sensing Mechanisms in MEMS-Based Sensor Devices. *Nanoscale Research Letters*, 16(1):16, January 2021.

[3] Daniel Platz and Ulrich Schmid. Vibrational modes in MEMS resonators. *Journal of Micromechanics and Microengineering*, 29(12):123001, October 2019. Publisher: IOP Publishing.

[4] Haoran Wang, Yifei Ma, Qincheng Zheng, Ke Cao, Yao Lu, and Huikai Xie. Review of Recent Development of MEMS Speakers. *Micromachines*, 12(10):1257, October 2021. Number: 10 Publisher: Multidisciplinary Digital Publishing Institute.

[5] Philipp Moll. *Bistable SiC MEMS membranes: the potential for medical applications*. Thesis, Wien, 2020. Accepted: 2020-06-27T20:58:47Z.

[6] Johannes Fabian. *Numerical simulation of parametrically excited bistable MEMS plates*. Thesis, Wien, 2022. Accepted: 2022-09-12T11:18:41Z.

[7] Masoud Derakhshani and Thomas A. Berfield. Snap-Through and Mechanical Strain Analysis of a MEMS Bistable Vibration Energy Harvester. *Shock and Vibration*, 2019:e6743676, March 2019. Publisher: Hindawi.

[8] Nan Hu and Rigoberto Burgueño. Buckling-induced smart applications: recent advances and trends. *Smart Materials and Structures*, 24(6):063001, May 2015. Publisher: IOP Publishing.

[9] M. Dorfmeister, M. Schneider, and U. Schmid. 3D characterisation of piezoelectric bistable MEMS membranes during switching. *Sensors and Actuators A: Physical*, 298:111576, October 2019.

[10] M. Dorfmeister, B. Kössl, M. Schneider, G. Pfusterschmied, and U. Schmid. Switching performance of bistable membranes activated with integrated piezoelectric thin film transducers. *Journal of Micromechanics and Microengineering*, 29(10):105008, August 2019. Publisher: IOP Publishing.

[11] Lawrence N. Virgin. Plates. In *Vibration of Axially-Loaded Structures*, pages 183–215. Cambridge University Press, September 2007.

[12] J. Dolbow and M. Gosz. Effect of out-of-plane properties of a polyimide film on the stress fields in microelectronic structures. *Mechanics of Materials*, 23(4):311–321, August 1996.

[13] Fridtjov Irgens. *Continuum Mechanics*. Springer, Berlin, Heidelberg, 2008.

[14] S. Ilanko. Vibration and Post-buckling of In-Plane Loaded Rectangular Plates Using a Multiterm Galerkin's Method. *Journal of Applied Mechanics*, 69(5):589–592, August 2002.